IMPORTANCE OF FLUID COMPRESSIBILITY AND MULTI-PHASE FLOW IN NUMERICAL MODELING OF HYDRAULIC FRACTURE PROPAGATION

A Thesis

by

JAEYOUNG PARK

Submitted to the Office of Graduate and Professional Studies of
Texas A&M University
in partial fulfillment of the requirements for the degree of

MASTER OF SCIENCE

Chair of Committee,	Jihoon Kim
Committee Members,	George J. Moridis
	Zenon Medina-Cetina
Head of Department,	Dan Hill

August 2016

Major Subject: Petroleum Engineering

ABSTRACT

We employ the semi-analytical approach in modeling of coupled flow and geomechanics, where flow is solved numerically and geomechanics is solved analytically. We first model a PKN hydraulic fracture geometry numerically and incorporate the fluid compressibility term in order to investigate the effect of the fluid compressibility on hydraulic fracture geometry evolution. The results show that as the fluid becomes compressible, the fracture propagation is delayed because it takes time for pressure to be built up to extend the fracture. In a multi-phase flow system, we model a hydraulic fracturing process in a gas reservoir by solving flow numerically and geomechanics analytically. The fracture propagates slowly when water saturation of the reservoir is low. This implies high initial gas saturation, resulting in high total compressibility of reservoir fluid. We observe the gas concentration near the fracture tip, caused by (1) the movement of initial gas within the fracture to the fracture tip and (2) the possibility of the leakage of gas from the formation to the hydraulic fracture. The existence of gas is another factor that can lead fluid flow within the hydraulic fracture to be compressible.

DEDICATION

To my lovely wife, Haemin

ACKNOWLEDGEMENTS

I would like to thank my committee chair, Dr. Jihoon Kim, who provided me with opportunity, financial support and tremendous guidance to complete my master program. Sincere thanks to my other committee members, Dr. George J. Mordis, and Dr. Zenon Medina-Cetina for their guidance during the course of this research. I am also thankful to Dr. Minsu Cha for his attendance in my final examination substituting for Dr. Medina-Cetina.

Special thanks to all my friends and classmates for inspiring and encouraging me during course works and discussions on issues that I have. With their help, I was able to make it through and finish my work.

NOMENCLATURE

c_t	Total compressibility
k	Permeability
q	Flow rate
t	Time
u	Darcy flux
p	Pressure
v	poisson’s ratio
A	Cross sectional area
G	Shear modulus
H	Fracture thickness
L	Length

Subscripts

f	Fluid
g	Gas
net	Net
i	Space index
inj	Injected
n	Time index
ref	Reference
w	Water

Superscripts

$\dot{}$	Time derivative

Greek variables and operators

γ	Shape factor
θ	Moving coordinate
μ	Fluid viscosity
ρ	Density
ϕ	Porosity
Δ	Difference
∇	Gradient

TABLE OF CONTENTS

Page

LIST OF FIGURES

Page

LIST OF TABLES

Page

CHAPTER I

INTRODUCTION*

The scientific community has made several assumptions in the research of hydraulic fracturing. One assumption is to neglect the effects of fluid compressibility by assuming that the fracturing fluid is incompressible, one of the main assumptions in analytical solutions of hydraulic fracturing geometry. Still, considering the magnitude of the stiffness of a typical rock and the stiffness of the injected fluid (such as water), the effects of the fluid compressibility should not be ignored. Furthermore, when the fracturing fluid is gas, such as nitrogen or carbon dioxide, the compressibility of the fluid must be considered to account for the geomechanical changes in the reservoir. Another common assumption is to disregard that gas in a gas reservoir is going to infiltrate the hydraulic fracture from the reservoir formation during hydraulic fracturing operations, whereas leak-off from the hydraulic fracture into the reservoir formation is usually considered. Note that some studies have indicated that the existence of a gap between the fracture tip and the water front is possible. This gap implies the possibility of leakage of shale gas from the formation into the hydraulic fracture.

*Part of the material in this section is reprinted from "Importance of fluid compressibility and multi-phase flow in numerical modeling of hydraulic fracture propagation" by Park, J., Kim, J., 2016, June. presented at the 50th ARMA symposium.

In order to investigate the importance of fluid compressibility in the hydraulic fracturing process, we first focus on modeling a Perkins-Kern-Nordgen fracture geometry which is first introduced by Perkins and Kern (1961) and further improved by Nordgren (1972). A PKN geometry has been considered to be physically acceptable in a sense that the fracture length is larger than its height, which is one of the primary assumptions of the geometry. Once we validate our numerical modeling comparing the numerical results with analytical solutions, we derive mass balance equations assuming the fluid is not incompressible to incorporate fluid compressibility in the equations.

To demonstrate the hydraulic fracturing process in multi-phase flow systems, we solve multi-phase flow numerically, but geomechanics analytically by using modified fixed-stress split scheme. In the fixed-stress split method, fluid flow part is solved first, fixing the total stress fields, and then geomechanics is updated from the variables obtained from the flow part at the previous time step (Kim et al., 2011). This sequential method shows high accuracy and unconditional numerical stability, and furthermore can easily be conducted in the existing flow simulators by updating a porosity function and its correction term. (Kim et al., 2011, Kim et al., 2012a, Kim et al., 2012b).

We conduct numerical simulations for a highly gas-saturated reservoir with very low permeability and porosity. The gas represents pure methane in this study so that all the properties, such as the critical pressure temperature, the acentric factor and the molecular weight, of pure methane are utilized to calculate viscosity and density of gas in the simulations. We investigate the fracture propagation speed varying initial water saturation of the reservoir. We also investigate water saturation at the fracture tip to see

the gas concentration which implies the possibility of the leakage of gas from the formation to the hydraulic fracture.

CHAPTER II

HYDRAULIC FRACTURE PROPAGATION MODEL IN SINGLE-PHASE FLOW

In this chapter, we review assumptions and governing equations used in a PKN hydraulic fracture geometry. We solve the governing equations numerically by discretizing the equations in terms of time and space and compare it with the analytical solution for PKN hydraulic fracture geometry. In order to save computational costs, a moving mesh algorithm is employed in numerical calculation introduced by Detournay et al. (1990). To account for the effect of the fracturing fluid, we derive governing equations assuming that the fluid is compressible.

Before moving to the mathematical statement, note that we refer to the governing equations in Detournay et al. (1990) in this study. Readers might be confused when they compare the equations in Detournay's paper with other materials since Detournay used q as flow rate per unit height of fracture. However, they are all in consistency and that confusing part is resulted from the fact that a PKN has an elliptical cross section in a vertical direction. It is also worth noting that a PKN fracture geometry has following main assumptions referring to Gidely et al. (1989), Valko and Economides (1995) and Economides and Nolte (2000).

- The fracturing height is considered to be fixed which is independent of the length.
- The fracturing fluid pressure holds constant in vertical cross sections
- The deformation of each vertical section is independent of each other.
- The cross section in vertical planes has an elliptical shape.

Note that $L(t)$ and $w(0,t)$ are considered to be total fracture length and maximum fracture width, respectively.

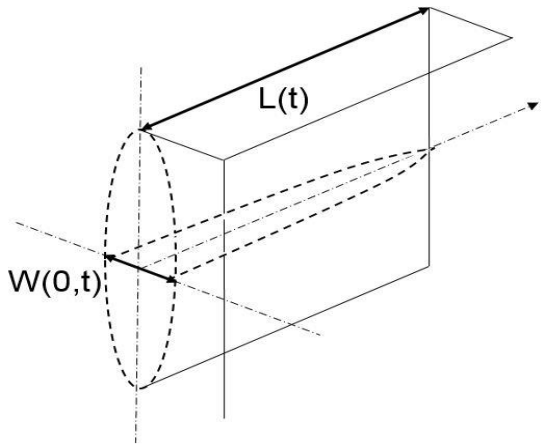

Figure 1. Schematic figure of a PKN fracture geometry.

2.1 Mathematical statement

2.1.1 Continuity equation

The continuity equation (i.e. local mass balance equation) for hydraulic fracture propagation models* is as follows:

$$\frac{\partial q}{\partial x}+\frac{\partial w}{\partial t}+u=0 \tag{1}$$

*Eq.(1) is applied not only to PKN but also to KGD hydraulic fracture geometry. This is because the principle of mass conservation in a local manner is identical in both fracture geometries.

where q is a flow rate per unit height of the fracture, w is the average fracture width and u is a fluid leak-off velocity. In an impermeable reservoir, there is no leak-off from the hydraulic fracture to the formation so that the leak-off term is neglected.

2.1.2 Fluid momentum balance equation

In a PKN fracture geometry, if we assume laminar flow of a Newtonian fluid in the direction of the fracture propagation, the fluid momentum balance equation becomes

$$q = -\frac{w^3}{\pi\mu}\frac{\partial p_f}{\partial x} \tag{2}$$

where p_f is the pressure in the fracture and μ is the viscosity of the fracturing fluid.

2.1.3 Pressure-width relation

The average fracture width is calculated by an elasticity in the state of plan strain:

$$p_{net} = \frac{4G}{\pi(1-v)H}w \tag{3}$$

where p_{net} is the effective stress, v is the Possion's ration and G is the shear modulus of the formation. H is the height of the fracture.

2.1.4 Global mass balance equation

The global mass balance equation is based on the principle that the total volume of the fracture is identical to the volume of fluid injected into the formation and the cumulative leak-off volume. It is represented as

$$\int_0^{L(t)} w(x,t)dx + \int_0^t \int_0^{L(t')} u(x,t)dxdt' - \int_0^t q_0(t')dt' = 0 \tag{4}$$

where q_0 is the injected fluid rate per unit height of the fracture. In impermeable reservoirs, assuming no leak-off term in the equation, the total injected volume is the same as the total fracture volume.

2.1.5 Initial and boundary condition

Demonstrating the PKN fracture geometry necessitates solving the equations with initial and boundary conditions. The problem is subject to the initial conditions:

$$w(x,0) = 0,\ L(0) = 0,\ p(0,0) = 0 \text{ at } t = 0 \tag{5}$$

and boundary conditions:

$$q(0,t) = q_0 \text{ for one-sided fracture}$$

$$p\big(L(t),t\big) = 0 \text{ for } t > 0 \tag{6}$$

$$w(x,t) = 0 \text{ for } x > L(t)$$

2.1.6 Moving coordinate system

Nilson and Griffiths (1983), Ramamurthy and Hujeux (1988) and Detournay et al. (1990) used a moving coordinate system to illustrate hydraulically-driven fracture problems. One of the advantages of using the moving coordinate system is that it enables running simulations with fixed number of locations. For example, with this system, the number of nodes at the initial time and at the end is the same regardless of the evolution of the total fracture length. Referring to Detournay et al. (1990), it is possible to transform the mathematical statements into the moving coordinate system θ:

$$\theta = x / L(t) \tag{7}$$

Basically, the moving coordinate system is the form of normalized coordinate along the fracture length so it has the range of [0, 1]. Time and spatial derivatives are converted in terms of θ as follows:

$$\left.\frac{\partial}{\partial t}\right|_x = \left.\frac{\partial}{\partial t}\right|_\theta - \frac{\theta \dot{L}}{L}\frac{\partial}{\partial \theta} \tag{8}$$

where $\dot{L} = dL/dt$ and

$$\left.\frac{\partial}{\partial x}\right|_t = \frac{1}{L}\left.\frac{\partial}{\partial x}\right|_\theta \tag{9}$$

The mathematical statements are transformed and presented in Table 1.

Table 1. Mathematical statements in x and θ coordinates

x coordinate	
$\frac{\partial q}{\partial x}+\frac{\partial w}{\partial t}+u=0$	(1)
$q=-\frac{w^3}{\pi\mu}\frac{\partial p_f}{\partial x}$	(2)
$\int_0^{L(t)} w(x,t)dx+\int_0^t\int_0^{L(t')} u(x,t)dxdt'-\int_0^t q_0(t')dt'=0$	(4)
$w(x,0)=0,\ L(0)=0,\ p(0,0)=0 \text{ at } t=0$	(5)
$q(0,t)=q_0,\ \ p(L(t),t)=0 \text{ for } t>0$ and $w(x,t)=0 \text{ for } x>L(t)$	(6)

θ coordinate	
$\frac{\partial w}{\partial t}-\frac{\theta\dot{L}}{L}\frac{\partial w}{\partial\theta}+\frac{1}{L}\frac{\partial q}{\partial\theta}+u=0$	(10)
$q=-\frac{w^3}{\pi\mu}\frac{1}{L}\frac{\partial p_f}{\partial\theta}$	(11)
$L\int_0^1 w(\theta,t)d\theta+\int_0^t L(t')\int_0^1 u(\theta,t')d\theta dt'-\int_0^t q_0(t')dt'=0$	(12)
$w(\theta,0)=0,\ L(0)=0,\ p(0,0)=0 \text{ at } t=0$	(13)
$q(0,t)=q_0,\ \ p(1,t)=0 \text{ for } t>0$ and $w(\theta,t)=0 \text{ for } \theta>1$	(14)

2.2 Numerical modeling

The equations in Sec.2.1 are solved numerically. An explicit finite difference method is utilized by discretizing the equations in terms of time and space to illustrate a

PKN geometry in a single-phase flow. An impermeable system of the reservoir is assumed to neglect the effect of leak-off. The following is how we discretize the equations and the algorithm used in our simulator. Also, a moving mesh algorithm is utilized to save computational costs.

2.2.1 Equations discretization

The equations are discretized by using explicit finite difference method. For the purpose of simplicity, we assume that there is no leak-off from the hydraulic fracture into the formation (i.e. $u = 0$). The coordinate, θ, is discretized into N nodes. At each node, pressure and fracture width (i.e. aperture, opening) are calculated and flow rate is computed between adjacent nodes. The schematic figure of space discretization are shown in Figure 2. In Figure 2, pressure and fracture width are calculated at the points of blue dots and flow rate is obtained at red dots.

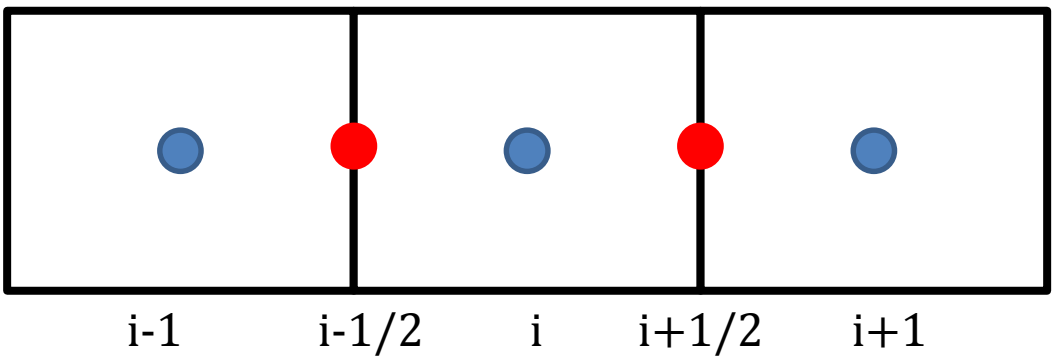

Figure 2. Schematic figure of space discretization

First of all, the continuity equation, Eq. (10), is discretized as follows (Detournay et al. 1990):

$$w_i^{n+1} = w_i^n + \Delta t^{n+1}\left(\frac{\theta_i \dot{L}^n}{L^n} \frac{w_{i+1}^n - w_i^n}{\theta_{i+1} - \theta_i} - \frac{2}{L^n} \frac{q_{i+1/2}^n - q_{i-1/2}^n}{\theta_{i+1} - \theta_{i-1}} \right) \text{ when } i = 2, N-1 \qquad (15)$$

And for the very first node,

$$w_1^{n+1} = w_i^n + \Delta t^{n+1}\left(-\frac{2}{L^n} \frac{q_{3/2}^n - q_0^n}{\theta_2} \right) \qquad (16)$$

And the last node

$$w_N^{n+1} = 0 \qquad (17)$$

In the fluid momentum balance equation, Eq. (11), in order to calculate the flow rate at mid-point nodes, the average of adjacent fracture width is used.

$$q_{i+1/2}^{n+1} = \frac{\left| p_i^{n+1} - p_{i+1}^{n+1} \right|}{p_i^{n+1} - p_{i+1}^{n+1}} \frac{1}{\pi \mu L^n} \left(\frac{w_i^{n+1} + w_{i+1}^{n+1}}{2} \right)^3 \times \frac{p_{i+1}^{n+1} - p_i^{n+1}}{\theta_{i+1} - \theta_i} \text{ when } i = 1, N-1 \qquad (18)$$

It is worth noting that q_0 always holds constant as we saw in boundary conditions unless we change the injection rate during the simulation. Therefore, q_0 is an input, not a variable which changes through simulation and it should go into Eq. (16). The pressure-width relation, Eq. (3), becomes

$$p_i^{n+1} = \frac{4G}{\pi(1-\nu)H} w_i^{n+1} \text{ when } i = 1, N \tag{19}$$

Note that p_f in Eq. (2) and p_{net} in Eq. (3) become identical assuming the initial state is in equilibrium so that both initial p_{net} and p_f are zero.

The total fracture length (i.e. $L(t)$ in Figure 1) is calculated by the principle of global mass balance: the total injected fluid volume should be equal to the volume of the hydraulic fracture. Here, we introduce the average fracture width, $\overline{w}$, and shape factor, γ. The definition of $\overline{w}$ is the ratio of the volume of the hydraulic fracture to the area of one face of the wing. To be specific, $\overline{w}$ is the width when we approximate the total fracture volume into a cuboid which has an equivalent volume as the fracture volume. γ is the ratio of $\overline{w}$ to w and is usually a value of $\pi/5$ in PKN fracture geometry*. Detournay et al. (1990) introduced the way we can obtain a shape factor in a moving coordinate system:

$$\gamma^{n+1} = \frac{\theta_2}{2} + \sum_{i=2}^{N-1} \frac{(\theta_{i+1} - \theta_i) \times w_i^{n+1}}{2w_1^{n+1}} - \frac{(1-\theta_{N-1})w_{N-1}^{n+1}}{6w_1^{n+1}} \tag{20}$$

*Please refer to Chapter 4 and 9 of Valko and Economides (1995) and Chapter 18 of Economides et al. (2012) for further information

If we have equally spaced nodes along θ, adding up fracture widths along the fracture at a certain time and dividing it by the number of nodes and maximum fracture width gives us similar results as a shape factor.

The fracture length is computed as follows:

$$L^{n+1} = \frac{V_{inj}^{n+1}}{\overline{w}^{k+1}} = \frac{V_{inj}^{n+1}}{w_1^{k+1}\gamma^{k+1}} \tag{21}$$

where V_{inj}^{n+1} is the total injected fluid volume at time step $n+1$, which is calculated by

$$V_{inj}^{n+1} = \sum_{k=1}^{n+1} q_0^k \Delta t^k = V_{inj}^n + q_0^{n+1}\Delta t^{n+1} \tag{22}$$

The fracture growth rate, $\dot{L}$, in Eq. (15) is computed as follows:

$$\dot{L}^{n+1} = \frac{\left(L^{n+1} - L^n\right)}{\Delta t^{n+1}} \tag{23}$$

2.2.2 Numerical stability

In general, numerical stability is one of the critical issues in solving non-linear equations by using an explicit method. In this study, we take the heuristic approach which is presented in Detournay et al. (1990) to investigate the numerical stability.

Taking a derivative of Eq. (3) with respect to x yields to

$$\frac{\partial p}{\partial x} = \frac{4G}{\pi(1-\nu)H}\frac{\partial w}{\partial x} \tag{24}$$

Then, Eq. (2)becomes,

$$q = -\frac{w^3}{\pi^2 \mu} \frac{4G}{\pi(1-\nu)H} \frac{\partial w}{\partial x} \tag{25}$$

Note that in Eq. (1), we have a derivative q with respect to x. To take a derivative Eq. (25) with respect to x becomes,

$$\frac{\partial q}{\partial x} = -\frac{4G}{\pi^3 \mu(1-\nu)H} \left(3w^2 \frac{\partial w}{\partial x} + w^3 \frac{\partial^2 w}{\partial x^2} \right) \tag{26}$$

Substituting Eq. (26) into Eq. (1) is now,

$$\frac{\partial w}{\partial t} = \frac{4G}{\pi^3 \mu(1-\nu)H} \left(3w^2 \frac{\partial w}{\partial x} + w^3 \frac{\partial^2 w}{\partial x^2} \right) \tag{27}$$

Using the coordinate transformation in Eq. (8) and Eq. (9), Eq. (27) becomes,

$$\frac{\partial w}{\partial t} = \frac{4G}{\pi^3 \mu(1-\nu)H} \frac{w^3}{L^2} \frac{\partial^2 w}{\partial \theta^2} + \frac{4G}{\pi^3 \mu(1-\nu)H} \frac{3w^2}{L^2} \left(\frac{\partial w}{\partial \theta} \right)^2 + \frac{\dot{\theta L}}{L} \frac{\partial w}{\partial \theta} \tag{28}$$

Here, we assume that the numerical stability only depends on the coefficient of the first term and the critical time step is computed as

$$\Delta t_{crit}^{n+1} = \min \left[\frac{\Delta \theta_i^2}{2} \frac{\pi^3 (1-\nu) \mu H (L^n)^2}{4G (w_i^n)^3} \right] \tag{29}$$

In the case that the grid is equally divided, put an arbitrary number such as 1 in i so that $\Delta\theta_i^2 = (\theta_2 - \theta_1)^2$ and $(w_i^n)^3 = (w_1^n)^3$.

2.2.3 Numerical algorithm

The program has the following algorithm.

1. The critical time step for the following iteration, Δt^{n+1}, is obtained from the numerical stability, Eq. (29), knowing the values of w_i, p_i, $q_{i+1/2}$, L and $\dot{L}$ at previous time step, $n+1$.

2. The fracture width at nodal points, w_i^{n+1} is calculated from the continuity equation, Eq. (15), with a given Δt^{n+1} in the previous procedure.

3. The fluid pressure along the fracture, p_i^{n+1}, is computed by using the pressure-width equation, Eq. (19).

4. The fluid flow rate between adjacent nodes, $q_{i+1/2}^{n+1}$, is calculated from the fluid momentum balance equation, Eq. (18).

5. The total fracture length is updated by employing the global mass balance equation, Eq. (21), while the shape factor γ^{n+1} is obtained from Eq. (20).

6. The fracture length growth rate, $\dot{L}^{n+1}$, is calculated from Eq. (23) and it goes into procedure 2 to calculate w_i at a new time step.

The schematic figure for the algorithm of the program is presented below.

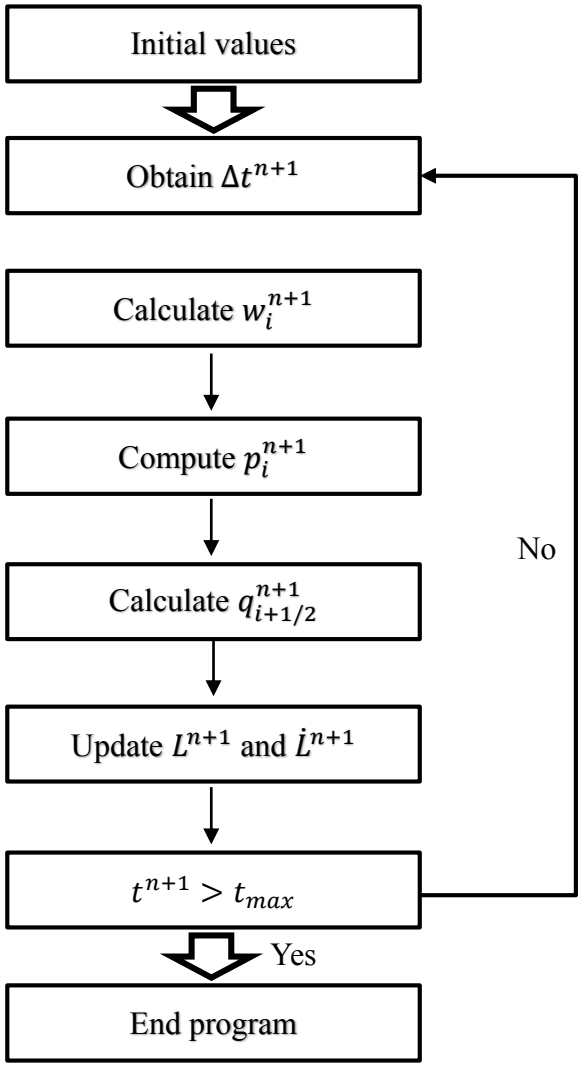

Figure 3. Schematic figure of the program algorithm

2.2.4 Verification of numerical model

The PKN numerical model has been verified with the approximation solution derived by Nordgren (1972). The numerical simulation domain is presented in Figure 4. We take a horizontal plane of the hydraulic fracture and demonstrate the half of the taken plane. In the figure, the blue arrow is the half of the maximum fracture width and the red arrow is the total fracture length. We assumed that there is no leak-off from the fracture to the formation for simplicity.

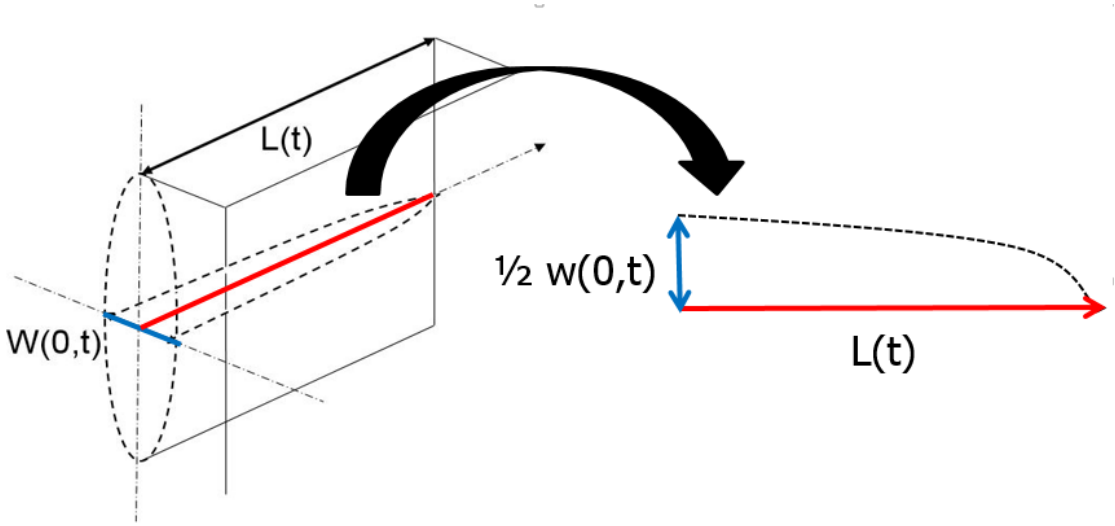

Figure 4. Numerical domain of PKN fracture geometry

For the analytical solution, we refer to the solutions in Gidley et al. (1989) which are presented in Table 2.

Table 2. The analytical solution for PKN fracture geometry

$w(0,t)$	$p(0,t)$	$L(t)$
$2.50\left(\frac{(1-\nu)q_o^2\mu}{GH}\right)^{1/5} t^{1/5}$	$\frac{2.75}{H}\left(\frac{Gq_o^3\mu L(t)}{(1-\nu)^3}\right)^{1/4}$	$0.68\left(\frac{Gq_o^3}{(1-\nu)\mu H^4}\right)^{1/5} t^{4/5}$

To conduct a sensitivity analysis on the number of nodes in the moving coordinate, θ, we run simulations varying the number of nodes. The fracture width profiles are presented in Figure 5 and the summary of the results is shown in Table 3. Note that the deviation in Table 3 is calculated by normalizing the value based on 50 nodes and the total simulation time is 1000 seconds.

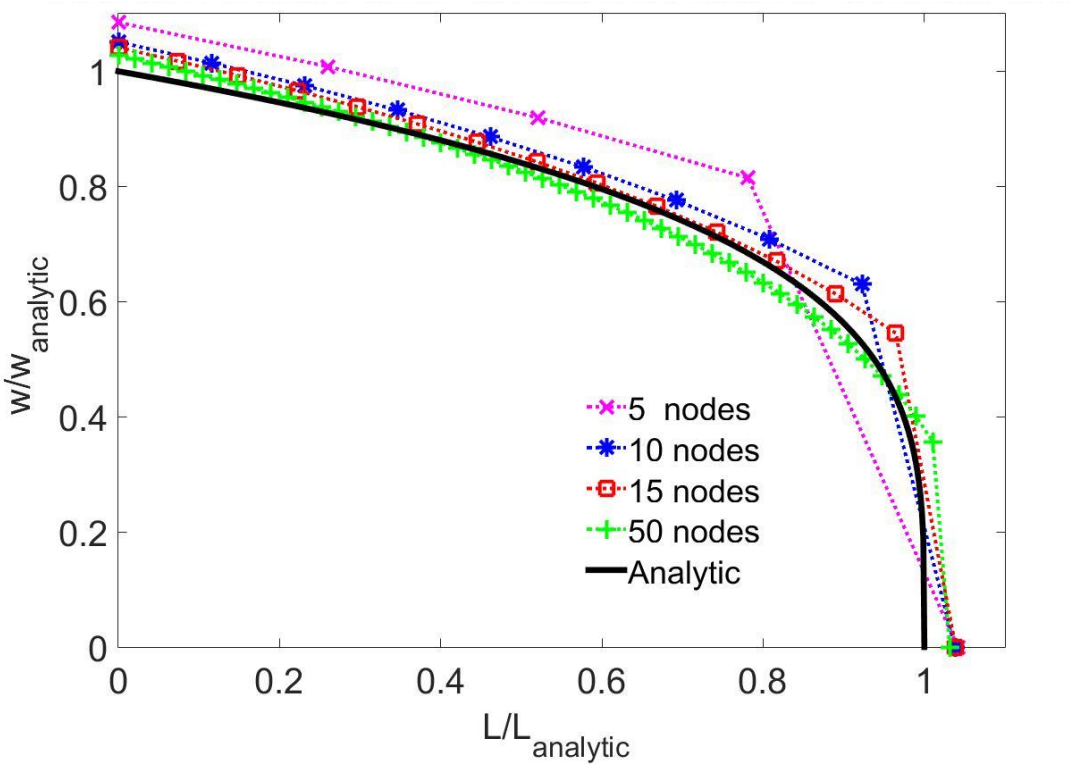

Figure 5. Fracture width profiles at different number of nodes

Table 3. Sensitivity analysis on the number of nodes

Number of nodes	Deviation in L	Deviation in $w_{\max}$	Running time(sec)
5	1.009	1.05	1.2
10	1.006	1.02	3.4
15	1.003	1.01	9
50	1	1	228

It is observed that fracture width becomes large when the number of nodes is small. However, total fracture length does not appear to vary in relation to the number of nodes in the moving coordinate system. When it comes to the simulation running time, it becomes exponentially larger, as shown in Figure 6, when the number of nodes is large. Therefore, we conclude that having the 15 nodes in the simulations gives reasonable results and less computational costs.

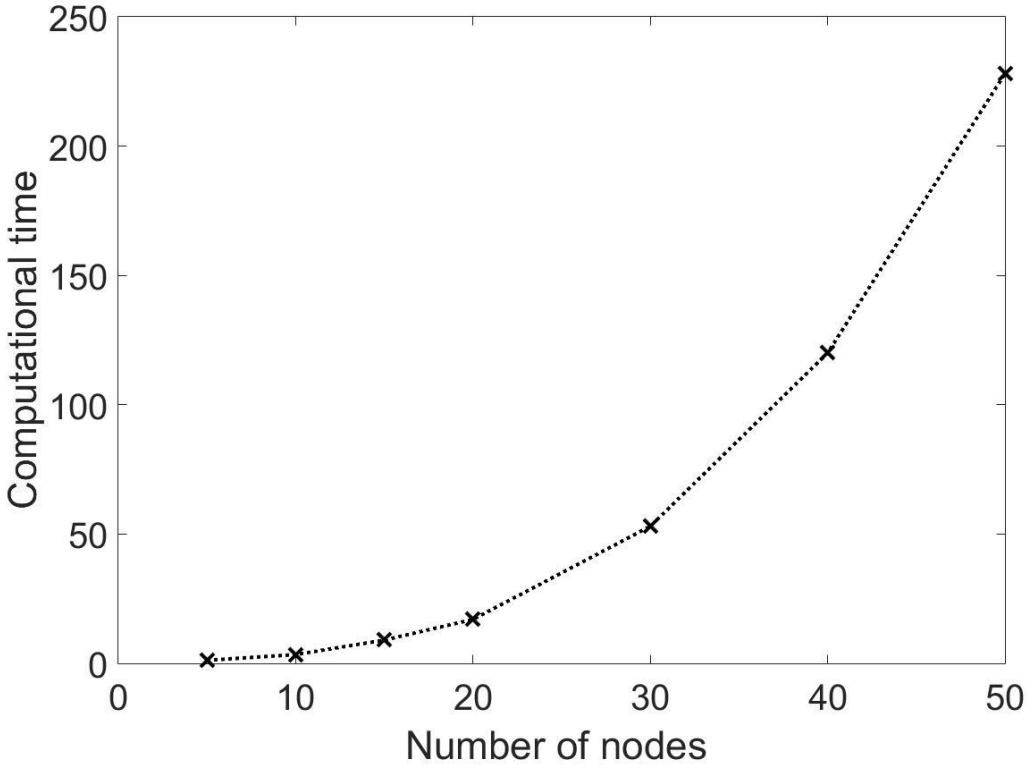

Figure 6. Increase in computational time with number of nodes

We run simulations with the parameters shown in Table 4 to compare the numerical results with analytical solutions. Note that this is the case without leak-off effect and that the fracturing fluid is incompressible.

Table 4. The parameters used in the simulation

Parameters	Value
Fluid viscosity (Pa·s)	5.6×10^{-1}
Injection rate (m^3/s)	4×10^{-3}
Possion's ratio	0.2
Shear modulus (GPa)	10
Fracture height (m)	1

The comparisons between the numerical results and the analytical solutions are presented in figures below.

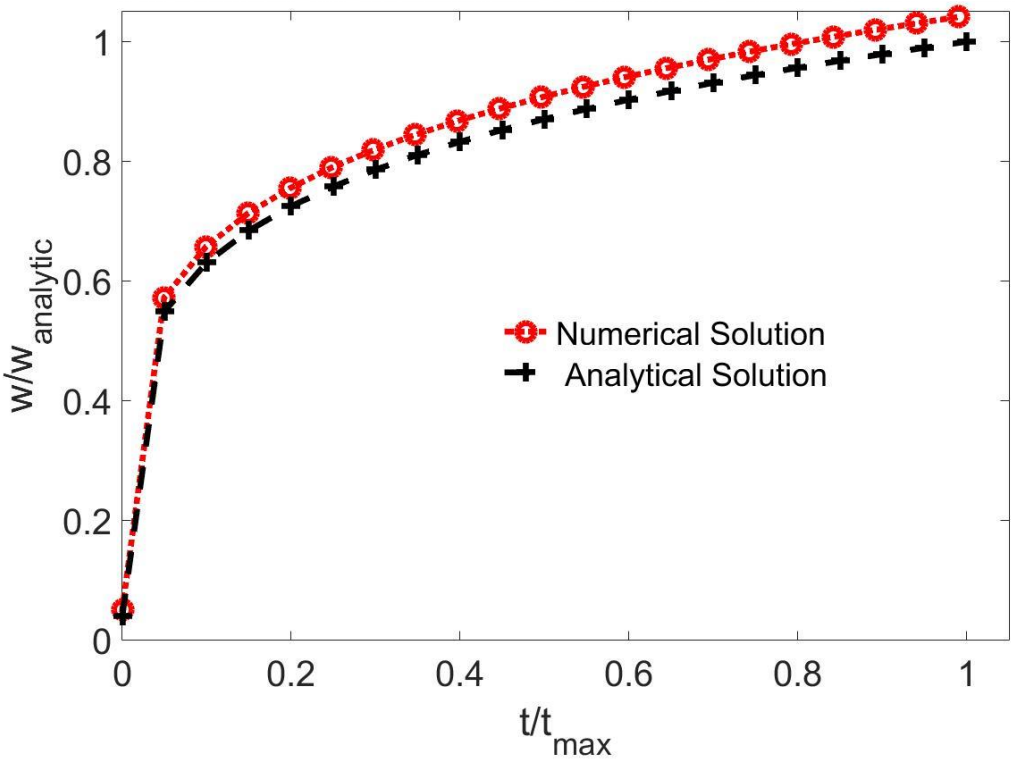

Figure 7. Numerical solution and the analytical solution in the fracture width

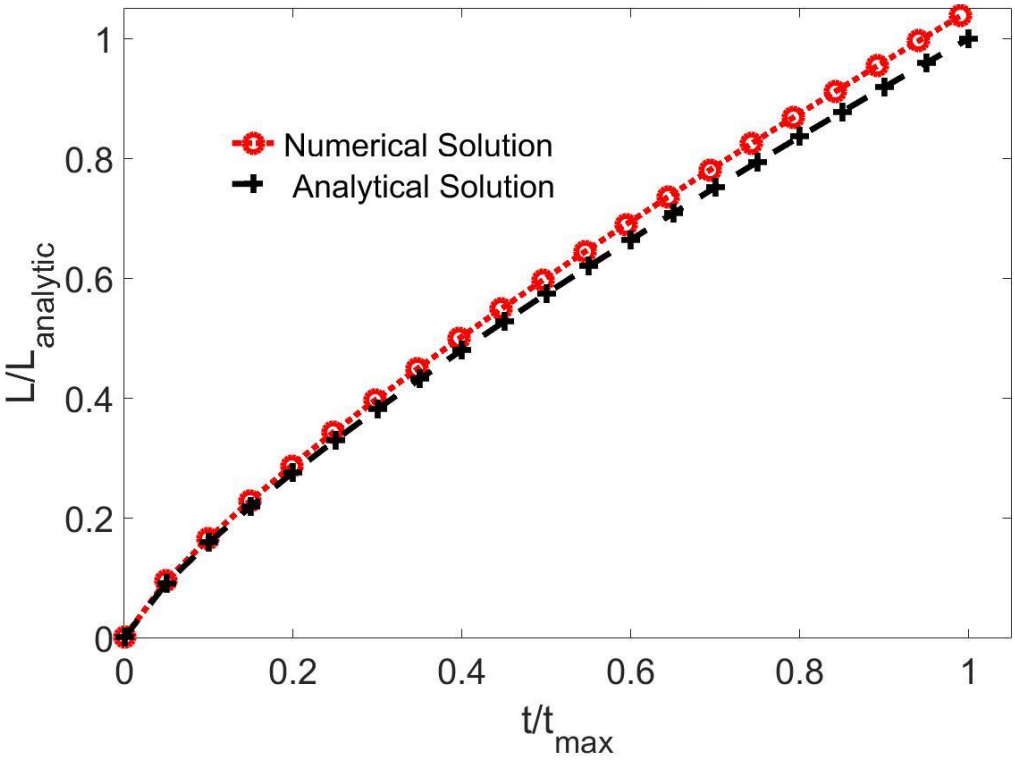

Figure 8. Numerical solution and the analytical solution in the fracture length

Note that axes are normalized. $w_{analytic}$ and $L_{analytic}$ are maximum value of analytical fracture width at wellbore and maximum value of analytical fracture length, respectively. $t_{\max}$ is total simulation time, $L_{\max}$ and $w_{\max}$ are and It is shown in Figure 8, that two solutions are matched up in both the fracture length and the fracture width at wellbore though small differences are observed at late time where numerical solutions are bigger than analytical solutions. It is worth noting that w in Eq. (1) indicates the average width of fracture, while in the analytical solution, $w(0,t)$ represents the maximum fracture width (i.e. fracture width at wellbore). Two widths are related to each other as

$w(0,t) = w \times 4/\pi$. It is shown that the numerical results are 3% and 5% larger than the analytical solutions in total fracture length and the maximum fracture width, respectively.

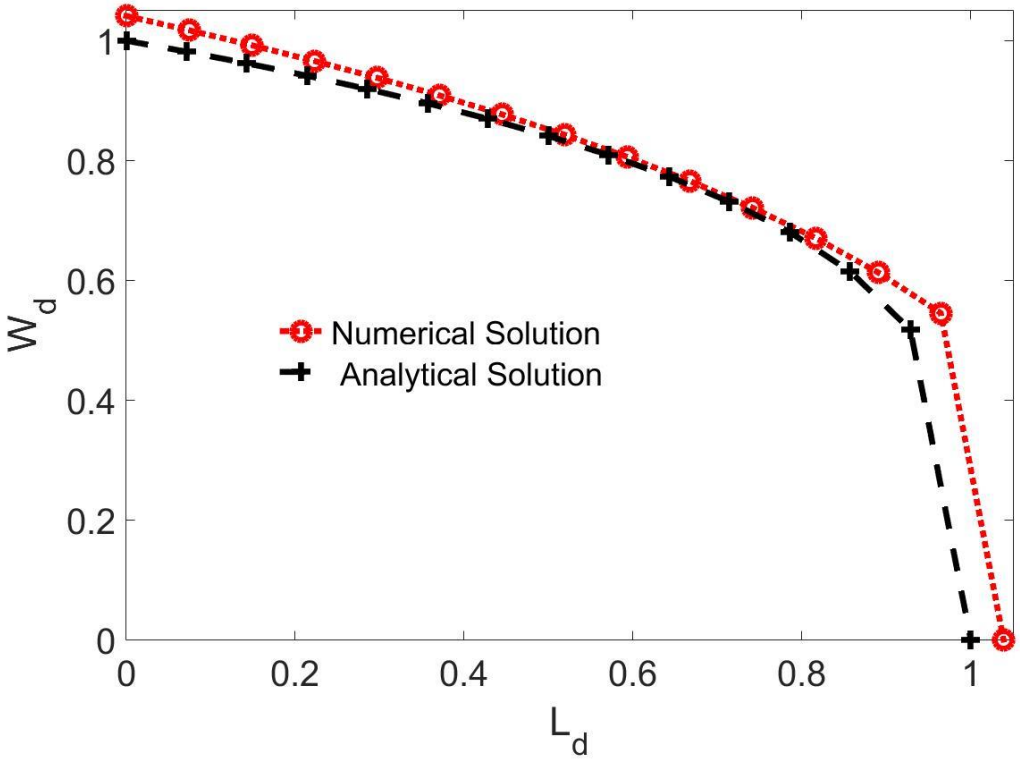

Figure 9. Fracture width profiles of numerical and analytical solutions

Figure 9 shows the fracture width profiles along the fracture from the numerical solution and analytical solution at the end time of the simulation. Referring to Gidley et al. (1989), the fracture profile can be analytically calculated with the maximum fracture width and the total fracture length as follows:

$$w(x) = w_{\max}\left(1 - \frac{x}{L_{\max}}\right)^{1/4} \tag{30}$$

where w_{max} and L_{max} are obtained from Table 2. To demonstrate the fracture profile from the numerical result, we take the fracture width values at the simulation end time. It is observed that the numerical fracture width at wellbore is larger than that from analytical solution as we see in Figure 8. When $L_d = 0.5 \sim 0.8$, the analytical fracture width is slightly larger than the numerical fracture width.

It is worth noting that, referring to Gidley et al. (1989), the fracture volume is calculated by

$$V = \frac{\pi}{5} LHw_{max} \tag{31}$$

By using Eq. (31), the fracture volume is calculated in a manner that V is larger than the injected volume. For example, with the parameters in Table 4, the analytical solutions in Table 2 give 115.7m for L and 0.0059m for w_{max} at 100 seconds of simulation time. Then V is 0.4289m^3. However, since the injection rate is 4×10^{-3} m^3/s, the injected volume should be 0.4m^3. I suppose that this gap results from assumptions of PKN fracture geometry. The volume comparison is presented below in Figure 10.

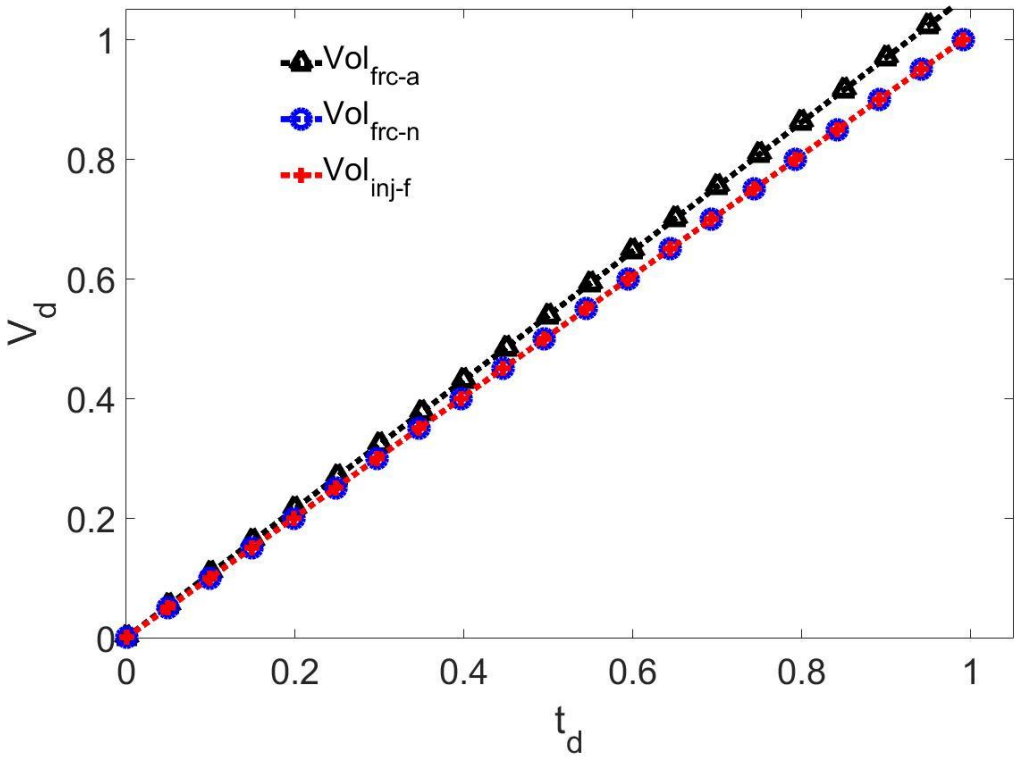

Figure 10. Comparison in analytic, numerical solution and injected volume

Note that Vol_{frc-a}, Vol_{frc-n}, and Vol_{inj-f} represent the fracture volume from analytical solutions, the volume from the numerical solution and the injected fluid volume. V_d is the volumes divided by the injected fluid volume and t_d is the simulation time divided by the total simulation time. The results show that the fracture volume by the numerical simulation is perfectly identical to the injected fluid volume. However, the analytical solution shows around 7% larger volume than the fluid volume.

2.3 Effect of fracturing fluid compressibility

2.3.1 Mass balance equations

To account for the effect of fluid compressibility, we utilize the concept of formation volume factor. The formation volume factor is defined as the ratio of the volume occupied by fluid at in-situ conditions (i.e. reservoir conditions) to that at standard conditions (i.e. surface conditions). It can be written in terms of the density of fluid:

$$B = \frac{\rho_{sc}}{\rho_{res}} = \frac{V_{res}}{V_{sc}} \tag{32}$$

where ρ_{sc} and ρ_{res} are the density of the fluid at standard conditions and at reservoir conditions, respectively. The formation volume factor for slightly compressible fluids (e.g. water, dead-oil) in isothermal systems might be approximated as follows (Ertekin et al., 2001):

$$B = \frac{B_{ref}}{1 + c_f (p - p_{ref})} \tag{33}$$

where B_{ref} is the formation volume factor at reference condition, p_{ref} is the pressure at reference condition and c_f is the compressibility of the fluid. We incorporate the formation volume factor in the continuity equation and the global mass balance equation to calculate the average fracture width and fracture length respectively at a specific time. Assuming that the fluid is compressible, the formation volume factor does not change with

space and that there is no leak-off from the fracture to the formation, the continuity equation can be derived as follows (detailed derivation is presented in the Appendix):

$$\frac{\partial q}{\partial x} + c_f w \frac{\partial p}{\partial t} + \frac{\partial w}{\partial t} = 0 \tag{34}$$

Note that width and pressure have a linear relation as shown in Eq. (3). Therefore, Eq. (32) is possibly written as

$$\left(\frac{4G}{\pi(1-\nu)H} + c_f w \right) \frac{\partial p}{\partial t} + \frac{\partial q}{\partial x} = 0 \tag{35}$$

The terms in Eq. (35) are expressed in a moving coordinate system, θ

$$\begin{aligned} \left. \frac{\partial q}{\partial x} \right|_t &= \frac{1}{L} \left. \frac{\partial q}{\partial \theta} \right|_t \\ \left. \frac{\partial p}{\partial t} \right|_x &= \left. \frac{\partial p}{\partial t} \right|_\theta - \frac{\theta \dot{L}}{L} \frac{\partial p}{\partial \theta} \end{aligned} \tag{36}$$

Therefore, Eq. (35) is written in a moving coordinate system as follows:

$$\left(\frac{4G}{\pi(1-\nu)H} + c_f w \right) \left(\frac{\partial p}{\partial t} - \frac{\theta \dot{L}}{L} \frac{\partial p}{\partial \theta} \right) + \frac{1}{L} \frac{\partial q}{\partial \theta} = 0 \tag{37}$$

The mass balance in the global manner assuming no leak-off effect is

$$V_{fracture} = V_{fluid,res} = L\int_0^1 w(\theta,t)d\theta - \int_0^t q_0(t') \times B(t')dt' \tag{38}$$

where $V_{fracture}$ is the volume of the hydraulic fracture and $V_{fluid,res}$ is the fluid volume at reservoir conditions.

2.3.2 Equation discretization

The equations with fluid compressibility are discretized by using explicit finite difference method as we do in Sec.2.2.1. No leak-off from the fracture into the formation (i.e. $u = 0$) is assumed and a moving coordinate, θ, is utilized.

Let us divide Eq. (37) by term1 and term2 and discretize them as follows:

$$\text{term1:}\ \ \frac{\dot{\theta L}}{L}\frac{\partial p}{\partial \theta} = \frac{\theta_i \dot{L}^n}{L^n}\frac{p_{i+1}^n - p_i^n}{\theta_{i+1}^n - \theta_i^n} \tag{39}$$

and

$$\text{term2:}\ \ \frac{1}{L}\frac{\partial q}{\partial \theta} = \frac{2}{L^n}\frac{q_{i+1/2}^n - q_{i-1/2}^n}{\theta_2} \ \text{ when } i = 2, N-1 \tag{40}$$

For the very first node, Term2 becomes

$$\text{Term2:}\ \ \frac{1}{L}\frac{\partial q}{\partial \theta} = \frac{2}{L^n}\frac{q_{3/2}^n - q_0}{\theta_2} \tag{41}$$

Therefore, discretized Eq. (37) is now

$$p_i^{n+1} = p_i^n + \Delta t\left(\text{Term1} + \text{Term2} \times \left(\frac{4G}{\pi(1-\nu)H} + c_f w_i^n\right)\right) \tag{42}$$

With a calculated p_i^{n+1} from Eq. (42), w_i^{n+1} is updated from the pressure-width relation:

$$w_i^{n+1} = \frac{\pi(1-\nu)H}{4G} p_i^{n+1} \tag{43}$$

The fluid momentum equation is the same as that in Sec.2.2.1, as well as shape factor equation. The total fracture length is computed as:

$$L^{n+1} = \frac{V_{inj,res}^{n+1}}{\overline{w}^{k+1}} = \frac{V_{inj,res}^{n+1}}{w_1^{k+1}\gamma^{k+1}} \tag{44}$$

where $V_{inj,res}^{n+1}$ is the total injected fluid volume at the reservoir condition at $n+1$ time step. The $V_{inj,res}^{n+1}$ is expressed as

$$V_{inj,res}^{n+1} = \sum_{k=1}^{n+1} q_0^k \Delta t^k B^k = V_{inj,res}^n + q_0^{n+1}\Delta t^{n+1} B^{n+1} \tag{45}$$

where B is the formation volume factor which is calculated from Eq. (33)

$$B^{n+1} = \frac{B_{ref}}{1 + c_f \left(p^{n+1} - p_{ref} \right)} \tag{46}$$

and p^{n+1} is the average pressure along the hydraulic fracture at the $n+1$ time step.

2.3.3 Numerical algorithm

In order to account for the effect of the fluid compressibility in hydraulic fracture geometry evolution, the program has the following algorithm.

1. The critical time step for the following iteration, Δt^{n+1}, is obtained from the numerical stability, Eq. (29), knowing that the values of w_i, p_i, $q_{i+1/2}$, L and $\dot{L}$ at previous time step, $n+1$.

2. The fluid pressure along the fracture, p_i^{n+1} is computed by using Eq. (37)-(40) knowing the values of $L, q, w, \dot{L}$ at previous time step and Δt^{n+1} in the previous procedure.

3. The fracture width at nodal points, w_i^{n+1} is calculated from the pressure-width relation, Eq. (41).

4. The fluid flow rate between adjacent nodes, $q_{i+1/2}^{n+1}$, is calculated from the fluid momentum balance equation, Eq. (18).

5. The total fracture length is updated by employing the global mass balance equation, Eq. (42), while the shape factor γ^{n+1} is obtained from Eq. (20).

6. The fracture length growth rate, $\dot{L}^{n+1}$, is calculated from Eq. (23) and it goes into procedure 2 to calculate p_i at new time step.

Comparing the equation above with the algorithm in Sec.2.2.3, we calculate the pressure first and then compute the fracture width. The reason that we change the sequence of the calculation is that we confront a numerical stability issue when we stick to the calculation of the fracture width first.

The schematic figure for the algorithm of the program is presented below.

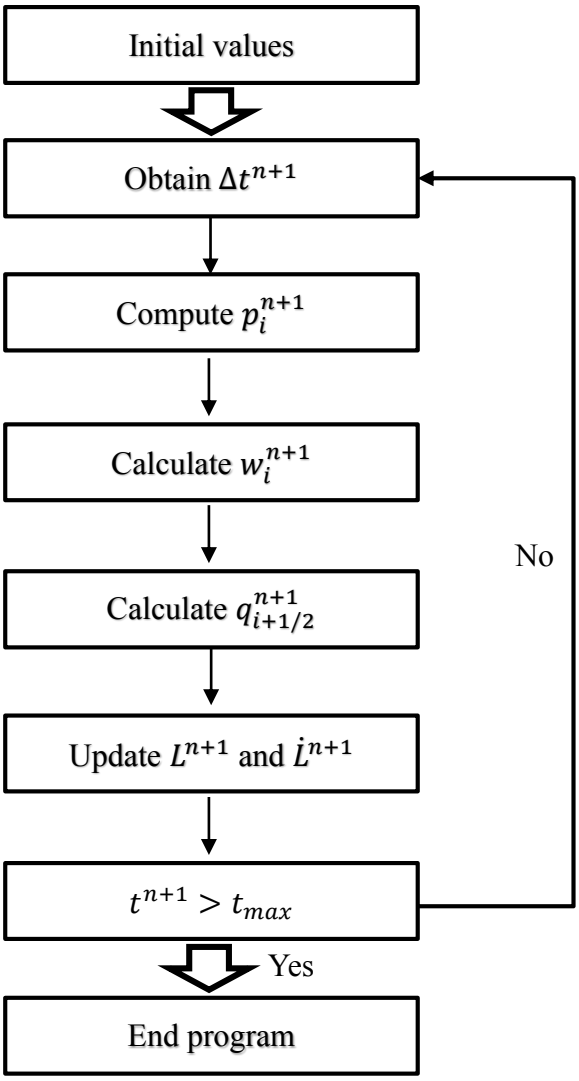

Figure 11. Schematic of the program algorithm with the fluid compressibility

2.3.4 Numerical results

When the assumption of incompressible fracturing fluid is lifted, the continuity equation and the global mass balance equation should incorporate the fluid compressibility effect. The reference conditions in Eq. (31) is the initial pressure so that the initial formation volume factor is identical to B_{ref} which is unity in the simulations. We implement simulations varying the fluid compressibility from 0 to 10^{-7} Pa^{-1}. The results are shown in Figure 11 Fluids can be classified as incompressible when the fluid compressibility is 0, slightly compressible when the fluid compressibility is approximately 10^{-10} Pa^{-1} to 10^{-9} Pa^{-1} or compressible when the fluid compressibility is larger than 10^{-8} Pa^{-1} (Ertekin et al., 2001). Therefore, in Figure 11, the pink line indicates the case of incompressible fluids, the blue and green lines represent slightly compressible fluid cases and the others are compressible fluid cases. In general, the fluid compressibility changes according to the pressure when the fluid is compressible. However, we approximate the formation volume factor of compressible fluid cases roughly using Eq. (31), assuming compressibility holds constant during the hydraulic fracture process. This leads to higher value of the formation volume factor than real value based on Peng-Robinson cubic state of equation as shown in Figure 12 Note that the temperature in the calculations is set to 20 °C.

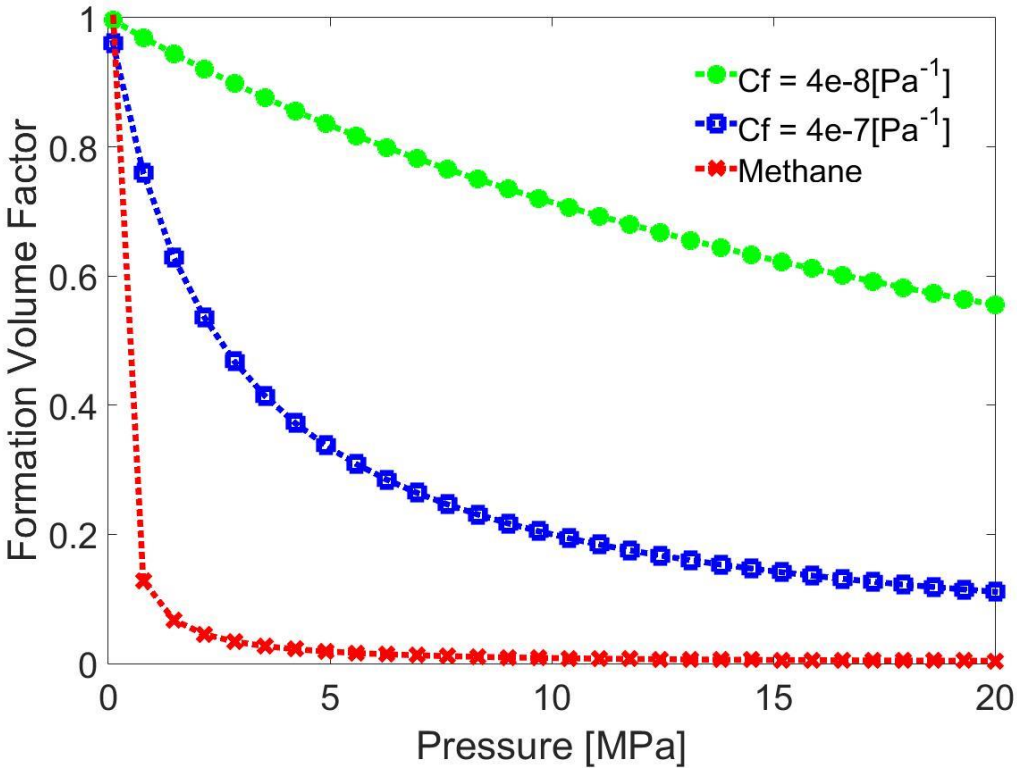

Figure 12. Formation volume factor with Peng-Robinson EOS and Eq. (46)

It is shown that the formation volume factor plunges with a small increase of the pressure whereas the formation volume factor from Eq. (31) decreases relatively smoothly. The final values also have significant differences: 0.5556, 0.1111, 0.0041 for the green, blue and red line, respectively. Recalling that the formation volume factor describes the ratio of the volume at the reservoir condition to the volume at the surface condition, this implies that the shrinkage effect of pressurized fluid is actually more significant than shown in these results. It is observed that as fluid becomes compressible, the fracture propagation is delayed. The fracture width also becomes smaller as the fluid

compressibility becomes larger. Note that we assume that the height is 1. When the simulation time increases, the difference in the fracture length and the fracture width become more significant.

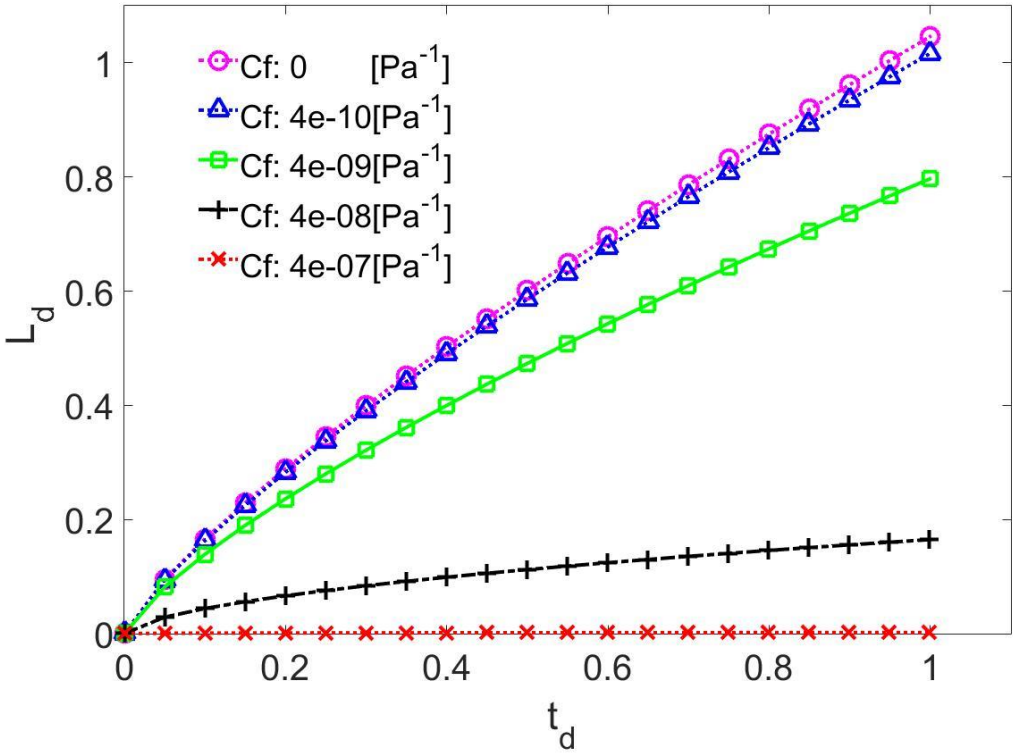

Figure 13. The fracture length at different fluid compressibilities

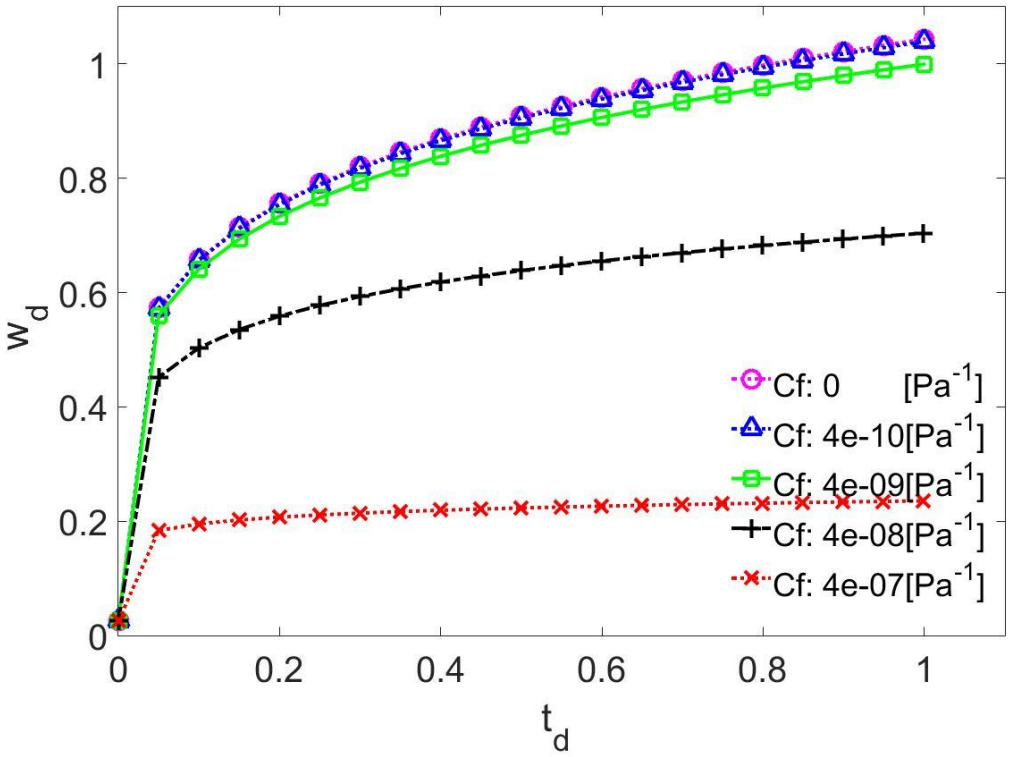

Figure 14. The maximum fracture width at different fluid compressibilities

Note that $L_{\max}$ and $w_{\max}$ values are utilized from the zero compressibility case to normalize the scales. The normalized results are presented in Table 5 below.

Table 5. The results of fracture geometry evolution at different fluid compressibilities

Compressibility	Maximum fracture width	Total fracture length
$c_f = 0$	1	1
$c_f = 4\times10^{-10}[Pa^{-1}]$	0.9971	0.9880
$c_f = 4\times10^{-09}[Pa^{-1}]$	0.9729	0.8900
$c_f = 4\times10^{-08}[Pa^{-1}]$	0.8048	0.3645
$c_f = 4\times10^{-07}[Pa^{-1}]$	0.3361	0.0095

Table 5 shows that as the compressibility of the fluid increases, both the fracture length and the width decrease. When the fluid compressibility is $4\times10^{-09}\text{Pa}^{-1}$, the total length of the fracture is reduced by more than 10% than that of the case when compressibility is 0. However, in terms of width, it only shows approximately 3% of drop off. Based on the numerical results, the fluid compressibility affect relatively huge on the total fracture length but not on the fracture width. This is also observed in the fracture width profile. Figure 15 shows the fracture width profiles at different fluid compressibilities. Based on the figure, the total fracture length shows relatively significantly change compared with the maximum fracture width.

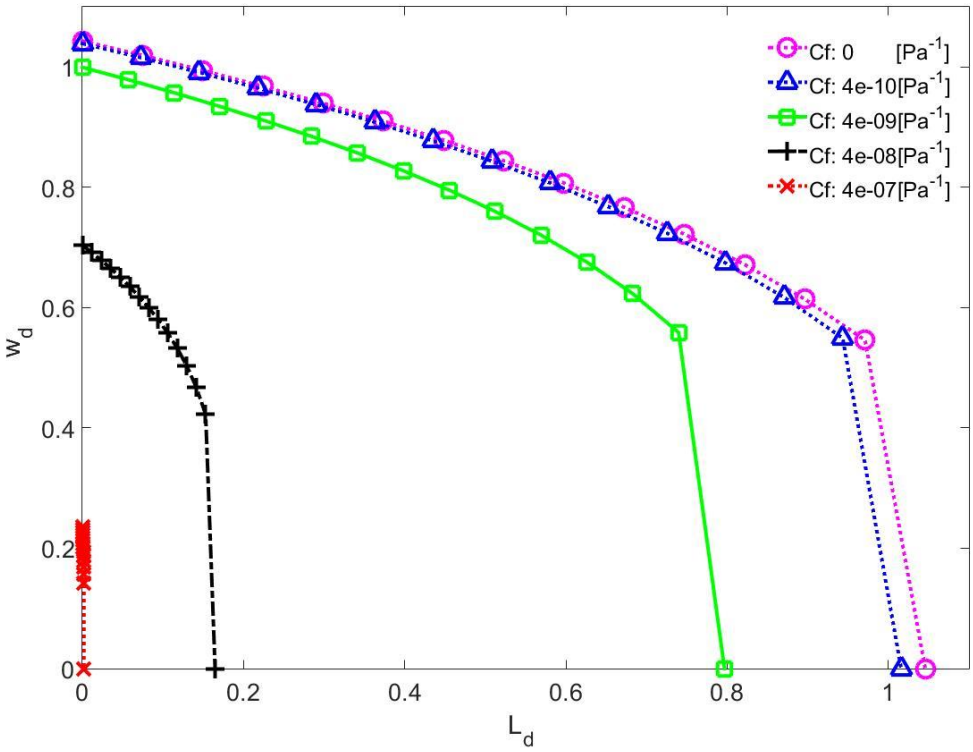

Figure 15. The fracture width profile at different fluid compressibility

CHAPTER III

HYDRAULIC FRACTURE MODEL IN MULTI-PHASE FLOW *

To demonstrate the hydraulic fracture propagation process in a gas reservoir, we utilize multi-phase flow through porous media to obtain pressure distribution in the reservoir and geomechanics model to determine fracture propagation and fracture width. We make an assumption that the system is isothermal. In this study, gas represents pure methane so that all the properties of pure methane, such as critical pressure and temperature and acentric factor, are utilized. We solve multi-phase flow numerically but geomechanics analytically by using a modified fixed-stress split scheme (Kim et al., 2011) in order to account for poromechanics within the fracture. This sequential method shows high accuracy and unconditional numerical stability, and furthermore can easily be conducted in the existing flow simulators by updating a porosity function and its correction term. (Kim et al., 2011, Kim et al., 2012a, Kim et al., 2012b)

*Part of the material in this section is reprinted from "Importance of fluid compressibility and multi-phase flow in numerical modeling of hydraulic fracture propagation" by Park, J., Kim, J., 2016, June. presented at the 50th ARMA symposium.

3.1 Mathematical statement

3.1.1 Single-phase fluid through porous media

The governing equation to describe the fluid flow through porous media is called the diffusion equation. To derive the diffusion equation, we have to begin with the principle material balance and combine Darcy's Law and an equation that demonstrates the fluid storage effect in porous media. Here, we first illustrate the case that one-dimensional fluid flow without source term for simplicity purpose. We employ a prismatic region in Figure 16 to show the principle of mass conservation. Note that q is volumetric flow per unit area and A is a cross-sectional area. The cross-sectional area does not change with the space in a one-dimensional flow system.

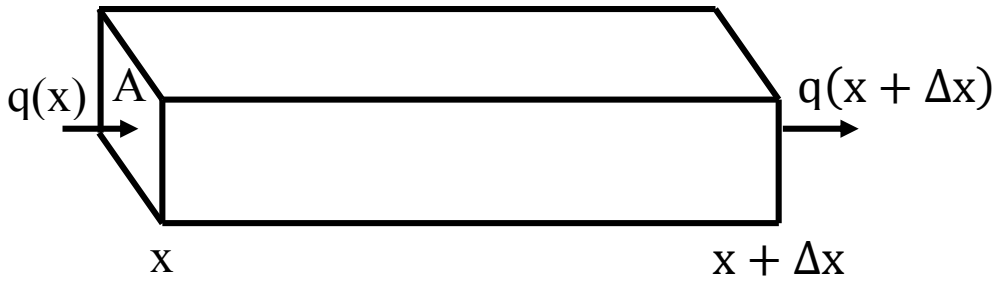

Figure 16. Schematic figure to describe the principle of mass conservation.

The idea is that the net mass flux from the prismatic region should be identical to the mass stored in the volume. Note that, in the figure, fluid is flowing from left to right. Let us indicate time lapse from t to t+Δt then,

Mass flux in: $\Delta t\left(q(x)\rho(x)A\right)$

Mass flux out: $\Delta t\left(q(x+\Delta x)\rho(x+\Delta x)A\right)$

Stored Mass: $m(t+\Delta t)-m(t)$

where $m=\rho\phi V=\rho\phi A\Delta x$. The mass balance equations is now written as:

$$\Delta t\left[q(x)\rho(x)A-q(x+\Delta x)\rho(x+\Delta x)A\right]=m(t+\Delta t)-m(t) \tag{47}$$

We can cancel out A from both side and divide it by Δt and Δx. Letting $\Delta t\to 0$ and $\Delta x\to 0$ yield to

$$\frac{\left[q(x)\rho(x)-q(x+\Delta x)\rho(x+\Delta x)\right]}{\Delta x}=\frac{\rho(t+\Delta t)\phi(t+\Delta t)-\rho(t)\phi(t)}{\Delta t} \tag{48}$$

and this is identical to

$$-\frac{\partial(\rho q)}{\partial x}=\frac{\partial(\rho\phi)}{\partial t} \tag{49}$$

The first term of Eq. (49) is expanded by using Darcy's Law,

$$q = \frac{Q}{A} = -\frac{k}{\mu}\frac{\partial p}{\partial x} \tag{50}$$

Note that q in Eq. (50) has unit of $[L/T]$. Then, the first term of Eq. (49) becomes

$$-\frac{\partial(\rho q)}{\partial x} = -\frac{\partial}{\partial x}\left(-\rho\frac{k}{\mu}\frac{\partial p}{\partial x}\right) = \frac{k}{\mu}\left(\rho\frac{\partial^2 p}{\partial x^2} + \frac{\partial\rho}{\partial x}\frac{\partial p}{\partial x}\right) \tag{51}$$

By using a chain rule, the last term in Eq. (51) is expressed as

$$\frac{k}{\mu}\left(\rho\frac{\partial^2 p}{\partial x^2} + \frac{\partial\rho}{\partial x}\frac{\partial p}{\partial x}\right) = \frac{k}{\mu}\left(\rho\frac{\partial^2 p}{\partial x^2} + \frac{\partial\rho}{\partial p}\frac{\partial p}{\partial x}\frac{\partial p}{\partial x}\right) = \frac{k}{\mu}\left(\rho\frac{\partial^2 p}{\partial x^2} + \frac{\partial\rho}{\partial p}\left(\frac{\partial p}{\partial x}\right)^2\right) \tag{52}$$

Note that the definition of the compressibility of the fluid (i.e. fluid compressibility) and the compressibility of the rock formation (i.e. pore compressibility) are following:

fluid compressibility (c_f): $$c_f = \frac{1}{\rho}\frac{\partial\rho}{\partial p} \tag{53}$$

pore compressibility (c_ϕ): $$c_\phi = \frac{1}{\phi}\frac{\partial\phi}{\partial p} \tag{54}$$

If we manipulate the last term in Eq. (52) and equate it with Eq. (53), it becomes

$$\rho\frac{k}{\mu}\left(\frac{\partial^2 p}{\partial x^2}+\frac{1}{\rho}\frac{\partial\rho}{\partial p}\left(\frac{\partial p}{\partial x}\right)^2\right)=\rho\frac{k}{\mu}\left(\frac{\partial^2 p}{\partial x^2}+c_f\left(\frac{\partial p}{\partial x}\right)^2\right) \tag{55}$$

Now, we expand the first term of Eq. (49) as

$$\frac{\partial(\rho\phi)}{\partial t}=\rho\frac{\partial\phi}{\partial t}+\phi\frac{\partial\rho}{\partial t} \tag{56}$$

By using a simple chain rule, Eq. (56) is expressed as

$$\rho\frac{\partial\phi}{\partial t}+\phi\frac{\partial\rho}{\partial t}=\rho\frac{\partial\phi}{\partial p}\frac{\partial p}{\partial t}+\phi\frac{\partial\rho}{\partial p}\frac{\partial p}{\partial t} \tag{57}$$

Recalling the definitions of the fluid compressibility and the pore compressibility, Eq. (57) is written as

$$\rho\phi\left[\left(\frac{1}{\phi}\frac{\partial\phi}{\partial p}\right)+\left(\frac{1}{\rho}\frac{\partial\rho}{\partial p}\right)\right]\frac{\partial p}{\partial t}=\rho\phi(c_\phi+c_f)\frac{\partial p}{\partial t} \tag{58}$$

Equate Eq. (55) and Eq. (58) results as the following

$$\frac{k}{\mu}\left(\frac{\partial^2 p}{\partial x^2}+c_f\left(\frac{\partial p}{\partial x}\right)^2\right)=\rho\phi(c_\phi+c_f)\frac{\partial p}{\partial t} \tag{59}$$

The second term on the left hand side is generally negligible since the magnitude of the value is around 10^{-4}~10^{-5} less compared to the first term. Therefore, the one-dimensional diffusion equation is

$$\frac{k}{\mu}\frac{\partial^2 p}{\partial x^2} = \rho\phi(c_\phi + c_f)\frac{\partial p}{\partial t} \tag{60}$$

For multi-dimensional systems, we have additional terms on the left hand side. For example, in three-dimensional Cartesian coordinate systems which can describe fluid flow in x, y and z direction, Eq. (60) is extended to

$$\frac{k}{\mu}\left(\frac{\partial^2 p}{\partial x^2} + \frac{\partial^2 p}{\partial y^2} + \frac{\partial^2 p}{\partial z^2}\right) = \rho\phi(c_\phi + c_f)\frac{\partial p}{\partial t} \tag{61}$$

3.1.2 Multi-phase flow through porous media

In order to describe a multi-phase flow system through porous media, we need an additional equation which governs the physics. First of all, the mass balance equation in Eq. (49) is applied in the multi-phase flow system as follows:

$$-\frac{\partial(\rho_l q_l)}{\partial x} = \frac{\partial(\rho_l \phi s_l)}{\partial t} \tag{62}$$

where l denotes the arbitrary phase of fluid, q_l is the volumetric flow of phase l per unit area and s_l is the saturation of phase l. Also, Darcy's Law in Eq. (48) is extended in multi-phase flow as follows:

$$q_l = -\frac{kk_{rl}}{\mu_l}\frac{\partial p_l}{\partial x} \tag{63}$$

where k is the absolute permeability, k_{rl} is the relative permeability of phase l, μ_l is the viscosity of phase l and p_l is the pressure of the phase l. Similarly, the compressibility term in Eq. (58) is to be extended to phase l:

$$\rho_l s_l \phi (c_\phi + c_l)\frac{\partial p_l}{\partial t} \tag{64}$$

where c_l is the compressibility of phase l and ρ_l is the density of phase l. Therefore, Eq. (60) is expressed in the multi-phase flow system as

$$\frac{kk_l}{\mu_l}\frac{\partial^2 p_l}{\partial x^2} = \rho_l \phi s_l (c_\phi + c_l)\frac{\partial p_l}{\partial t} \tag{65}$$

For example, in a water and gas flow system, we have two diffusion equations, one for water and the other for gas as shown below.

$$\frac{kk_w}{\mu_w}\frac{\partial^2 p_w}{\partial x^2} = \rho_w \phi s_w (c_\phi + c_w)\frac{\partial p_w}{\partial t} \tag{66}$$

$$\frac{kk_g}{\mu_g}\frac{\partial^2 p_g}{\partial x^2} = \rho_g \phi s_g (c_\phi + c_g)\frac{\partial p_g}{\partial t} \tag{67}$$

Now, we have four unknowns: p_w, p_g, s_w and s_g to solve the above equations. However, with the relationship between saturations

$$s_w + s_g = 1 \tag{68}$$

and pressures,

$$p_c(s_w) = p_g - p_w \tag{69}$$

we can induce two equations and two unknowns. In this study, p_g and s_w are selected to solve two-phase flow equations.

3.1.3 Gas - Equation of state

In order for us to calculate the gas viscosity and the formation volume factor of gas, we need to obtain the density of gas and the compressibility factor of gas, called the Z factor. The Z factor is a measure of how much the gas deviates from ideal gas behavior. The Z factor is the ratio of the volume actually occupied by a real gas at a given pressure and temperature to the volume that would be occupied by the ideal gas by definition.

$$z = \frac{V_{actual}}{V_{ideal}} \tag{70}$$

In this study, we employ the Peng and Robinson cubic equation of state to calculate the compressibility factor.

$$Z^3-(1-B)Z^2+\left(A-2B-3B^2\right)Z-\left(AB-B^2-B^3\right)=0 \tag{71}$$

In order to calculate the Z factor from the equation, we need to obtain parameters in the equation. The parameters are associated with the gas properties such as ideal gas constant, absolute temperature at the critical point, pressure at the critical point and the acentric factor of the gas and they are introduced below.

$$a=0.457235R^2\frac{T_c^2}{P_c} \tag{72}$$

$$b=0.077796R\frac{T_c}{P_c} \tag{73}$$

$$\alpha=\left(1+\kappa\left(1-T_r^{0.5}\right)\right)^2 \tag{74}$$

$$\kappa=0.37464+1.54226\omega-0.26692\omega^2 \tag{75}$$

$$A=\frac{a\alpha P}{R^2T^2} \tag{76}$$

$$B=\frac{bP}{RT} \tag{77}$$

where R is the ideal gas constant, T_c is the absolute temperature at the critical point, P_c is the pressure at the critical point, T_r is T/T_c and ω is the acentric factor of the gas. For pure methane, the properties have the following values:

Table 6. The properties of pure methane

R (J/(mol K)	T_c (K)	P_c (MPa)	ω	M (kg/mol)
8.31456	190.56	4.599	0.011	1.6043e-2

We are able to obtain the compressibility factor (or z factor) by solving Eq. (71). The values of the compressibility factor of methane at different temperatures are plotted below in Figure 17. The figure shows that the compressibility factor decreases until the pressure attains around 15 MPa. After 15 MPa, the compressibility factor increases with the increment in the pressure. The curvature of the curve diminishes when the temperature increase.

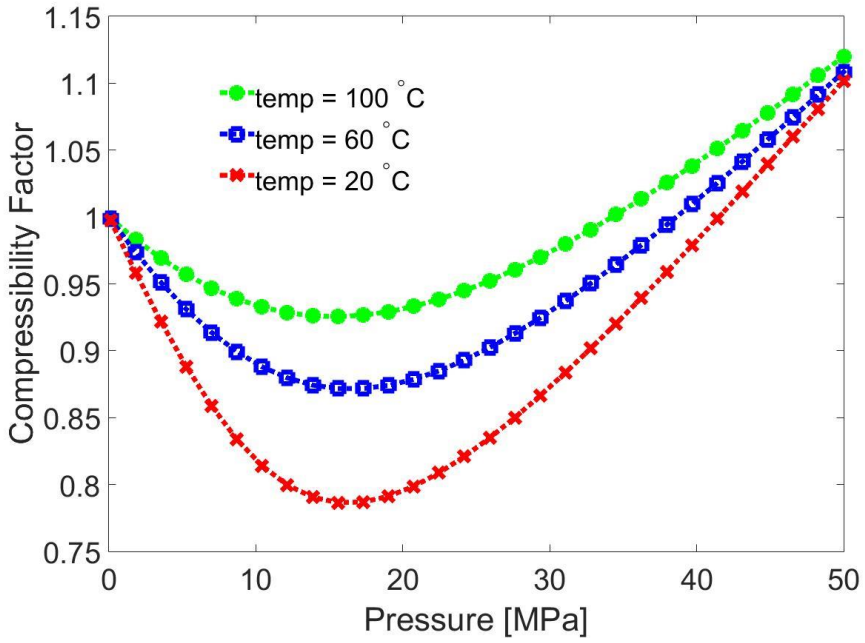

Figure 17. Compressibility factors of methane at different temperatures

The density of the gas can easily be obtained by

$$\rho_{gas} = P \times \frac{M}{RTZ} \tag{78}$$

where the unit of a density is in kg/m^3, T is the absolute temperature, P is Pa, R is 8.31 J/mol·K and M is the molecular weight of the gas and its unit is kg/mol. The densities of methane at different temperatures are presented below in Figure 18.

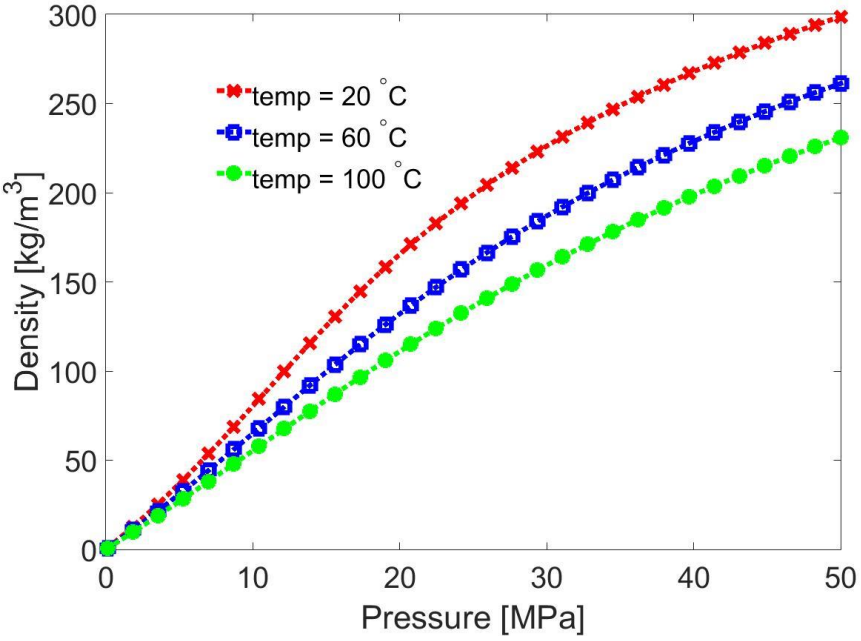

Figure 18. The densities of methane with pressure at different temperatures

We utilize the equation in the paper of Sun and Mohanty to calculate the viscosity of a gas. According to Sun and Mohanty (2005), the gas viscosity can be expressed as a function of the temperature and the gas density.

$$\mu_g = 2.4504\times10^{-3} + 2.8764\times10^{-5}T + 3.7838\times10^{-12}T + 2.0891\times10^{-5}\rho_g + 2.5127\times10^{-7}\rho_g^2 - 5.822\times10^{-10}\rho_g^3 + 1.8378\times\rho_g^4 \quad (79)$$

where ρ_g is the gas density and T is the absolute temperature of the gas. Since the gas density is a function of pressure, the viscosity can be described with pressure. The figure below indicates the changes of the gas viscosity with pressure at different temperatures. It

is shown in Figure 19 that when the temperature is higher, the viscosity of the gas changes less with the variation of pressure.

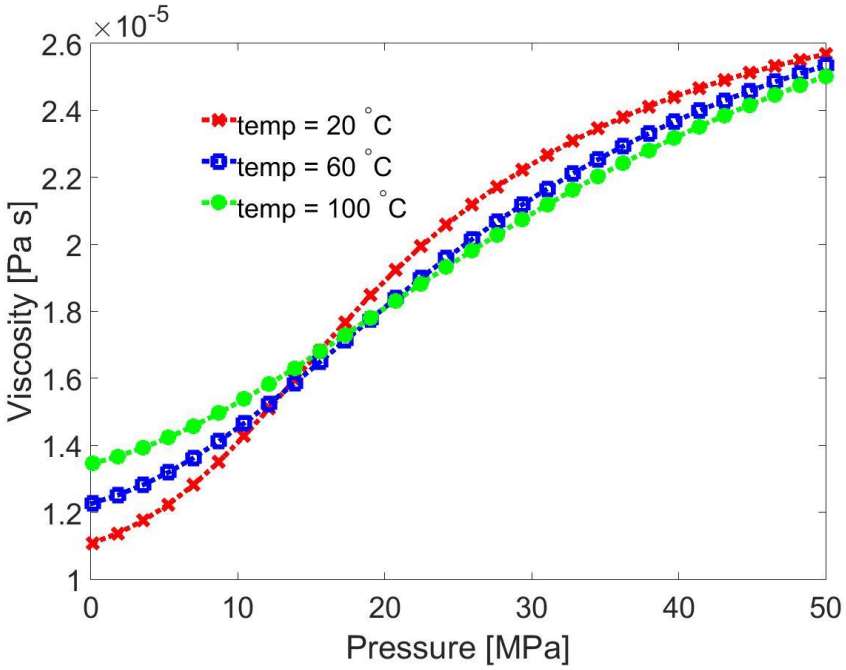

Figure 19. The viscosities of methane with pressure at different temperatures

3.1.4 Gas – Klinkenberg effect

Knudsen diffusion occurs when the mean-free-path of gas molecules is similar to the pore dimensions of the porous medium. Knudsen diffusion is only significant in porous media with very small pores (on the order of a few micrometers or smaller) and at low pressures. The phenomenon of Knudsen flow was first modeled and applied to petroleum engineering problems by Klinkenberg (1941). The correction for apparent gas permeability (Freeman et al., 2011) is:

$$k_a = k_o\left(1+\frac{b_k}{p}\right) \tag{80}$$

where k_a is the apparent or measured permeability in m^2, k_o is the intrinsic permeability of the porous medium in m^2, p is the pressure of the sample or reservoir in Pa and b_k is the Klinkenberg constant in Pa. Note that if we apply the definition of the Knudsen number and the mean-free-path, we show that Eq. (80) is equivalent to

$$k_a = k_0(1+4K_n) \tag{81}$$

and K_n is the Knudsen number and is expressed by

$$K_n = \frac{\bar{\lambda}}{r_{pore}} \tag{82}$$

where $\bar{\lambda}$ is the gas phase molecular mean-free-path in m, and r_{pore} is the characteristic length scale of the flow path in m.

3.1.5 Geomechanics - Fracturing criterion

The tensile strength is employed as large-scale fracture propagation criteria. In general, the fracture toughness is utilized for investigating small-scale fracture propagation (Adachi et al., 2007). According to Ruiz et al. (2000), Kim et al. (2013) and Kim et al. (2014), the tensile failure can occur when

$$\sqrt{|\mathbf{t}_s|^2/\beta^2 + t_n^2} \geq T_c \tag{83}$$

where $\mathbf{t}_s$ and t_n are the shear and normal traction and T_c is the tensile strength of the material. If $\beta \to \infty$, the tensile failure occurs due to normal traction, which is the case in this study. We simply assume that the failure occurs when the difference between hydraulic fluid pressure in the fracture and in-situ normal stress in the rock exceeds the tensile strength of the rock. Once the failure criteria is satisfied at a certain grid block, a new crack width is assigned at the grid block. The new crack width is accordingly determined by the crack width at the adjacent grid block.

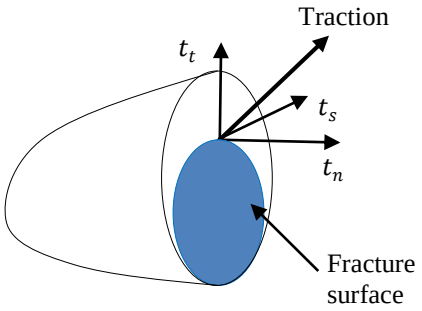

Figure 20. A schematic diagram for a planar fracture.

3.1.6 Geomechanics – Fracture width and permeability calculation

When a certain grid block is considered to be fractured, the fracture width at the grid block is calculated by using nonlocal elasticity relation (Sneddon and Lowengrub,

1969) with pressure distribution. Referring to Detournay (2004), nonlocal elasticity relation for $0 < x < L$ is written as:

$$w(x,t) = L\frac{1-\nu^2}{E}\int_0^1 p(sL,t)G_p(x/L,s)ds \tag{84}$$

where

$$G_p = -\frac{4}{\pi}\ln\left|\frac{\sqrt{1-\xi^2}+\sqrt{1-s^2}}{\sqrt{1-\xi^2}-\sqrt{1-s^2}}\right| \tag{85}$$

For the constant pressure distribution case (i.e. $p(sL,t) = p$), Eq. (85) becomes

$$w(x,t) = L(t)\frac{2(1-\nu)p}{G} \tag{86}$$

In order to calculate the permeability of the fracture, we utilize nonlinear permeability introduced by modified cubic law (Witherspoon et al., 1980; Rutqvist and Stephansson, 2003), for an example of one-dimensional single-phase fluid flow, written as

$$q = \alpha_c \frac{w^n}{12\mu}\left(\frac{\partial p}{\partial x} - \rho_f g\right) \tag{87}$$

where α_c is a coefficient accounting for the fracture roughness. Note that the equation becomes identical to the cubic law when $n = 3$ and $\alpha_c = 1$.

3.2 Numerical modeling

In this study, the fluid flow equation is discretized by the finite volume method and it is solved by using the fully implicit scheme with the Newton-Rapson method. However, the geomechanic part is updated by using analytical solutions introduced in the previous section. We solve two systems sequentially by updating information from each system to be used in another system. The schematic figure which shows how the program works is presented in Figure 21 below.

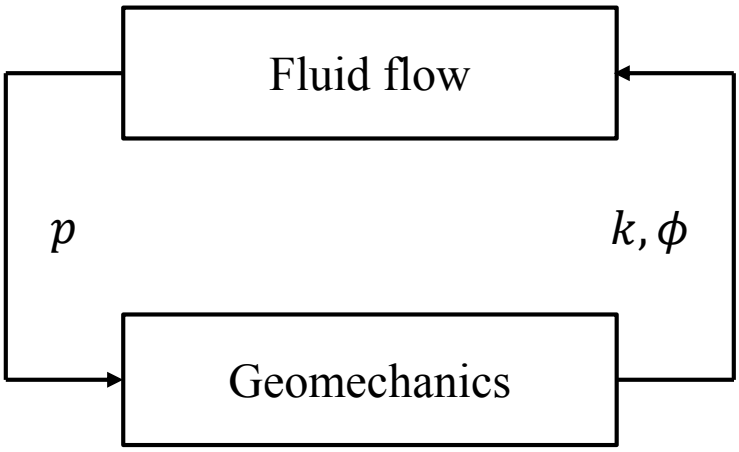

Figure 21. Schematic figure which shows sequential algorithm

3.2.1 Equations discretization

We have time derivative and space derivative with respect to fluid pressure in fluid flow equations. To discretize the equation we here introduce the basic element which is used for space discretization.

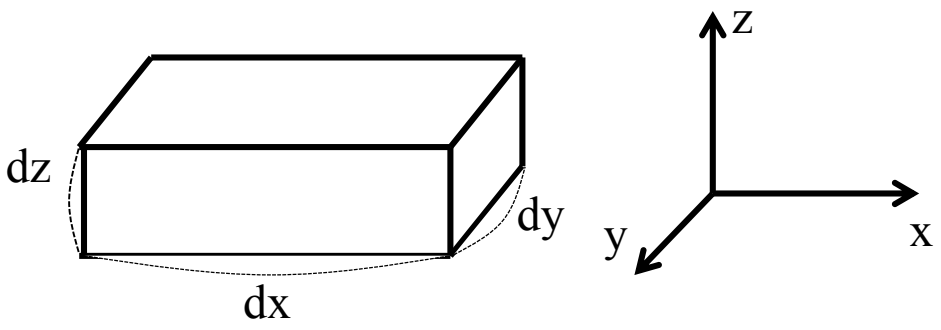

Figure 22. Schematic figure of an element in Cartesian coordinate.

To begin with, assuming 1D single-phase flow equation, it is discretized spatially only in x direction. With Eq. (32), Eq. (49) is also written as

$$-\frac{\partial}{\partial x}\left(\frac{k}{B\mu}\frac{\partial p}{\partial x}\right)=C\frac{\partial p}{\partial t} \tag{88}$$

where C is the total compressibility which is

$$C=\left(\frac{\phi}{B_o}c_f+\frac{\phi_o}{B}c_p\right) \tag{89}$$

The left hand side of Eq. (88) is discretized as follows:

$$\frac{1}{\Delta x_i}\left[\lambda_{i+1/2}\left(\frac{p_{i+1}-p_i}{\Delta x^+}\right)+\lambda_{i-1/2}\left(\frac{p_{i-1}-p_i}{\Delta x^-}\right)\right] \tag{90}$$

where Δx_i is the size of the grid block i, P_i is the pressure at the grid block i, Δx^+ is the distance between grid block i and $i+1$, Δx^- is the distance between grid block i and $i-1$ as shown in Figure 23.

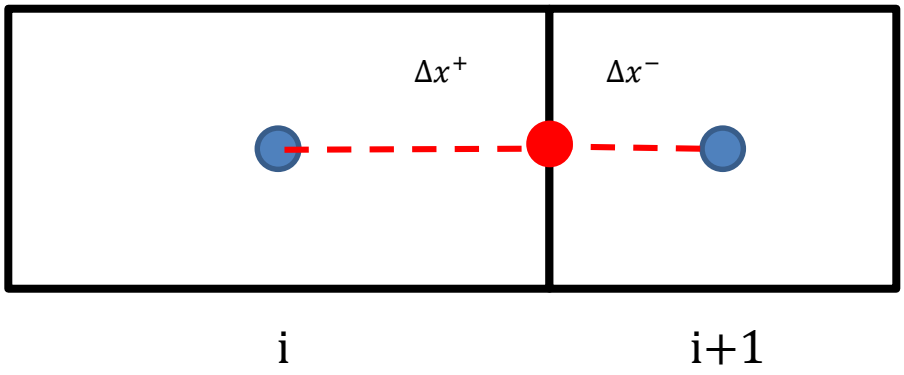

Figure 23 Schematic figure which shows distance between elements

and $\lambda_{i+1/2}$ is the mobility which is defined as a harmonic average of $\frac{k_i}{\mu_i B_i}$ and $\frac{k_{i+1}}{\mu_{i+1} B_{i+1}}$. The harmonic average is easily calculated as follows. Suppose we have $(A\times B/C)_i$ and $(A\times B/C)_{i+1}$. Then the harmonic average of these two becomes

$$\left(\frac{A\times B}{C}\right)_{i+1/2} = \frac{2}{\frac{1}{\left(\frac{A\times B}{C}\right)_i} + \frac{1}{\left(\frac{A\times B}{C}\right)_{i+1}}} = \frac{2A_iB_iA_{i+1}B_{i+1}}{A_iB_iC_{i+1} + A_{i+1}B_{i+1}C_i} \tag{91}$$

Meanwhile, the right hand side is discretized as

$$C\frac{\partial p}{\partial t} = C\frac{p_i^{n+1} - p_i^n}{\Delta t} \tag{92}$$

Equating Eq. (90) and Eq. (92) and multiplying by the volume of the element (i.e. $V_i = \Delta x_i \times \Delta y_i \times \Delta z_i$) shown in Figure 22 yield to

$$\left[A_{i+1/2}\lambda_{i+1/2}\left(\frac{p_{i+1} - p_i}{\Delta x^+} \right) - A_{i-1/2}\lambda_{i-1/2}\left(\frac{p_{i-1} - p_i}{\Delta x^-} \right) \right] = V_i C \frac{p_i^{n+1} - p_i^n}{\Delta t} \qquad (93)$$

where $A_{i+1/2}$ is a harmonic average of $\Delta y_i \cdot \Delta z_i$ and $\Delta y_{i+1} \cdot \Delta z_{i+1}$. In the fully implicit scheme, the time level at the left hand side of Eq. (93) is $n+1$. If a fully implicit scheme is employed and we have a source term at the i th element, Eq. (93) is rewritten as:

$$\left[A_{i+\frac{1}{2}}\lambda_{i+\frac{1}{2}}\left(\frac{p_{i+1}^{n+1} - p_i^{n+1}}{\Delta x^+} \right) - A_{i-\frac{1}{2}}\lambda_{i-\frac{1}{2}}\left(\frac{p_i^{n+1} - p_{i-1}^{n+1}}{\Delta x^-} \right) \right] = V_i C \frac{p_i^{n+1} - p_i^n}{\Delta t} + \tilde{q}_i \qquad (94)$$

where $\tilde{q}_i$ is the volumetric source term at i^{th} element and if it is producing, the sign of it is positive. When series of Eq. (94) is expressed in an expanded matrix form, it becomes:

LHS:

$$\begin{pmatrix} -\sum T - B_1 & T_E & \cdots & \cdots & \cdots & 0 \\ T_W & -\sum T - B_2 & T_E & \cdots & & \\ 0 & T_W & -\sum T - B_3 & T_E & \cdots & \\ & & & \vdots & & \\ & & & & \cdots\ T_W & -\sum T - B_{N-1} \quad T_E \\ 0 & & \cdots & \cdots & T_W & -\sum T - B_N \end{pmatrix} \begin{pmatrix} p_1^{n+1} \\ p_2^{n+1} \\ \vdots \\ p_{N-1}^{n+1} \\ p_N^{n+1} \end{pmatrix}$$

RHS:

$$-\begin{pmatrix} B_1 \\ B_2 \\ \vdots \\ B_{N-1} \\ B_N \end{pmatrix} \times \begin{pmatrix} p_1^n \\ p_2^n \\ \vdots \\ p_{N-1}^n \\ p_N^n \end{pmatrix} + Q$$

and in a simple way,

$$\left(\mathbf{T}^{n+1} - \mathbf{B}^{n+1}\right)\mathbf{P}^{n+1} = -\mathbf{B}^{n+1}\mathbf{P}^n + \mathbf{Q}^{n+1} \tag{95}$$

where $B_i = \dfrac{V_i C}{\Delta t}$.

In this study, we only consider two-phase, water and gas, fluid flow in porous media. From Eq. (62), we have two flow equations for water and gas. Water phase in one dimension, x, can be written similarly to Eq. (88):

$$-\frac{\partial}{\partial x}\left(k\frac{k_{rw}}{B_w\mu_w}\frac{\partial p_w}{\partial x}\right)=\frac{\partial(\phi s_w/B_w)}{\partial t} \tag{96}$$

It is worth noting that P_w can be expressed in terms of P_g and P_c from Eq. (69). Therefore, Eq. (96) is rewritten by expressing p_w as $p_o - p_c$:

$$-\frac{\partial}{\partial x}\left(k\frac{k_{rw}}{B_w\mu_w}\frac{\partial(p_o-p_c)}{\partial x}\right)=\frac{\partial(\phi s_w/B_w)}{\partial t} \tag{97}$$

Note that because p_c is the function of saturation, $\partial p_c/\partial x$ can be expressed as $\frac{\partial p_c}{\partial x}=\frac{\partial p_c}{\partial s_w}\frac{\partial s_w}{\partial x}$ by using the chain rule. However, in this study, we assume that the capillary pressure P_c is zero to make the problem simpler. As we choose p_o and s_w to be primary variables in two-phase flow equations, the right hand side of Eq. (97) should be expressed in the form of P_o and S_w as follows:

$$\left[\left(\frac{\phi}{B_w}s_w\right)^{n+1}-\left(\frac{\phi}{B_w}s_w\right)^{n}\right]= \\ \left[\frac{s_w^n}{B_w^{n+1}}\phi'+\frac{s_w^n}{B'_w}\phi'\right](p_o^{n+1}-p_o^n)+\left[\left(\frac{\phi}{B_w}\right)^{n+1}-s_w^n\phi^n\left(\frac{p_c}{B_w}\right)'\right](s_w^{n+1}-s_w^n) \tag{98}$$

where

$$\frac{1}{B_w^{'}} = \frac{(1/B_w)^{n+1} - (1/B_w)^n}{p_w^{n+1} - p_w^n} \tag{99}$$

$$p_c^{'} = \frac{p_c^{n+1} - p_c^n}{s_w^{n+1} - s_w^n} \tag{100}$$

$$\phi^{'} = \frac{\phi^{n+1} - \phi^n}{p_o^{n+1} - p_o^n} \tag{101}$$

and let us define $\frac{s_w^n}{B_w^{n+1}}\phi^{'} + \frac{s_w^n}{B_w^{'}}\phi^n = d_{11}$, $\left(\frac{\phi}{B_w}\right)^{n+1^{'}} - s_w^n \phi^n \left(\frac{p_c}{B_w^{'}}\right)^{'} = d_{12}$.

In gas phase flow, we have

$$\left[\left(\frac{\phi}{B_g} s_g\right)^{n+1} - \left(\frac{\phi}{B_g} s_g\right)^n\right] = -\left(\frac{\phi}{B_g}\right)^{n+1} (s_w^{n+1} - s_w^n) + (1 - s_w^n)\left[\frac{\phi'}{B_g^{n+1}} + \frac{\phi^n}{B'_g}\right](p_o^{n+1} - p_o^n) \tag{102}$$

where

$$\frac{1}{B_g^{'}} = \frac{(1/B_g)^{n+1} - (1/B_g)^n}{p_g^{n+1} - p_g^n} \tag{103}$$

$$\phi^{'} = \frac{\phi^{n+1} - \phi^n}{p_g^{n+1} - p_g^n} \tag{104}$$

and let us define $\left(1-s_w^n\right)\left(\frac{\phi^{'}}{B_g^{n+1}}+\frac{\phi^n}{B_g^n}\right)=d_{21},\ -\left(\frac{\phi}{B_o}\right)^{n+1}=d_{22}.$

Taken together from Eq. (96) to Eq. (104), the discretized equations can be expressed as the following matrix form:

$$\left(T^{n+1}-D^{n+1}\right)X^{n+1}=-D^{n+1}X^n+Q^{n+1}=0 \tag{105}$$

where X_i is a set of p_g and s_w. It is worth noting that since we have two equations for p_g and s_w, the matrix sizes of T^{n+1} and D^{n+1} are $2N\times 2N$ where N is the total number of grids in a system. In addition, the sizes of matrix X^{n+1} and Q^{n+1} are $2N\times 1$. When we expand Eq. (105) only from $i-1$ to $i+1$, it is shown as

$$\begin{pmatrix} (T_w)_{i-\frac{1}{2}}-(d_{11})_{i-\frac{1}{2}} & -(d_{12})_{i-\frac{1}{2}} & -\sum(T_w)_{i\pm\frac{1}{2}}-(d_{11})_i & -(d_{12})_i & (T_w)_{i+\frac{1}{2}}-(d_{11})_{i+\frac{1}{2}} & -(d_{12})_{i+\frac{1}{2}} \\ (T_g)_{i-\frac{1}{2}}-(d_{21})_{i-\frac{1}{2}} & -(d_{22})_{i-\frac{1}{2}} & -\sum(T_g)_{i\pm\frac{1}{2}}-(d_{21})_i & -(d_{22})_i & (T_g)_{i+\frac{1}{2}}-(d_{21})_{i+\frac{1}{2}} & -(d_{22})_{i+\frac{1}{2}} \end{pmatrix} \begin{pmatrix} (P_g)_{i-1}^{n+1} \\ (S_w)_{i-1}^{n+1} \\ (P_g)_i^{n+1} \\ (S_w)_i^{n+1} \\ (P_g)_{i+1}^{n+1} \\ (S_w)_{i+1}^{n+1} \end{pmatrix}$$

$$= \begin{pmatrix} -(d_{11})_{i-\frac{1}{2}} & -(d_{12})_{i-\frac{1}{2}} & -(d_{11})_i & -(d_{12})_i & -(d_{11})_{i+\frac{1}{2}} & -(d_{12})_{i+\frac{1}{2}} \\ -(d_{21})_{i-\frac{1}{2}} & -(d_{22})_{i-\frac{1}{2}} & -(d_{21})_i & -(d_{22})_i & -(d_{21})_{i+\frac{1}{2}} & -(d_{11})_{i+\frac{1}{2}} \end{pmatrix} \begin{pmatrix} (P_g)_{i-1}^{n} \\ (S_w)_{i-1}^{n} \\ (P_g)_i^{n} \\ (S_w)_i^{n} \\ (P_g)_{i+1}^{n} \\ (S_w)_{i+1}^{n} \end{pmatrix} + Q \tag{106}$$

3.2.2 Numerical algorithm

We utilize the Newton-Rapson method to solve the equation in the fully implicit scheme. The purpose of the Newton-Rapson method is to find the primary variable matrix which makes residual zero using Jacobian matrix. Jacobian matrix is obtained by taking the derivative of residual with respect to primary variables. In the single phase simulator,

$$J_{R(p)} = \begin{pmatrix} \frac{\partial R_1}{\partial p_1} & \frac{\partial R_1}{\partial p_2} & \cdots & \frac{\partial R_1}{\partial p_n} \\ \frac{\partial R_2}{\partial p_1} & \frac{\partial R_2}{\partial p_2} & \cdots & \frac{\partial R_2}{\partial p_n} \\ \vdots & \vdots & \ddots & \vdots \\ \frac{\partial R_n}{\partial p_n} & \frac{\partial R_n}{\partial p_n} & \cdots & \frac{\partial R_n}{\partial p_n} \end{pmatrix} \tag{107}$$

And in the two-phase simulator,

$$J_{R(p_g,s_w)} == \begin{pmatrix} \frac{\partial R_{g_1}}{\partial p_{g_1}} & \frac{\partial R_{g_1}}{\partial s_{w_1}} & \frac{\partial R_{g_1}}{\partial p_{g_2}} & \frac{\partial R_{g_1}}{\partial s_{w_2}} & \cdots & \frac{\partial R_{g_1}}{\partial p_{g_n}} & \frac{\partial R_{g_1}}{\partial s_{w_n}} \\ \frac{\partial R_{w_1}}{\partial p_{g_1}} & \frac{\partial R_{w_1}}{\partial s_{w_1}} & \frac{\partial R_{w_1}}{\partial p_{g_2}} & \frac{\partial R_{w_1}}{\partial s_{w_2}} & \cdots & \frac{\partial R_{w_1}}{\partial p_{g_3}} & \frac{\partial R_{w_1}}{\partial s_{w_n}} \\ \frac{\partial R_{g_2}}{\partial p_{g_1}} & \frac{\partial R_{g_2}}{\partial s_{w_1}} & \frac{\partial R_{g_2}}{\partial p_{g_2}} & \frac{\partial R_{g_2}}{\partial s_{w_2}} & \cdots & \frac{\partial R_{g_2}}{\partial p_{g_n}} & \frac{\partial R_{g_2}}{\partial s_{w_n}} \\ \frac{\partial R_{w_2}}{\partial p_{g_1}} & \frac{\partial R_{w_2}}{\partial s_{w_1}} & \frac{\partial R_{w_2}}{\partial p_{g_2}} & \frac{\partial R_{w_2}}{\partial s_{w_2}} & \cdots & \frac{\partial R_{w_2}}{\partial p_{g_n}} & \frac{\partial R_{w_2}}{\partial s_{w_n}} \\ \vdots & \vdots & \vdots & \vdots & \ddots & \vdots & \vdots \\ \frac{\partial R_{g_n}}{\partial p_{g_1}} & \frac{\partial R_{g_n}}{\partial s_{w_1}} & \frac{\partial R_{g_n}}{\partial p_{g_2}} & \frac{\partial R_{g_n}}{\partial s_{w_2}} & \cdots & \frac{\partial R_{g_n}}{\partial p_{g_2}} & \frac{\partial R_{g_n}}{\partial s_{w_n}} \\ \frac{\partial R_{w_n}}{\partial p_{g_1}} & \frac{\partial R_{w_n}}{\partial s_{w_1}} & \frac{\partial R_{w_n}}{\partial p_{g_2}} & \frac{\partial R_{w_n}}{\partial s_{w_2}} & \cdots & \frac{\partial R_{w_n}}{\partial p_{g_2}} & \frac{\partial R_{w_n}}{\partial s_{w_n}} \end{pmatrix} \tag{108}$$

Once we find the Jacobian matrix, we repeat the process to find a relatively small number, which is called tolerance, from the residual term ($\delta = -R/J$). In this study, the value of 10^{-6} is used for tolerance. A schematic algorithm of the Newton-Rapson method in single-phase flow is shown in Figure 24 below.

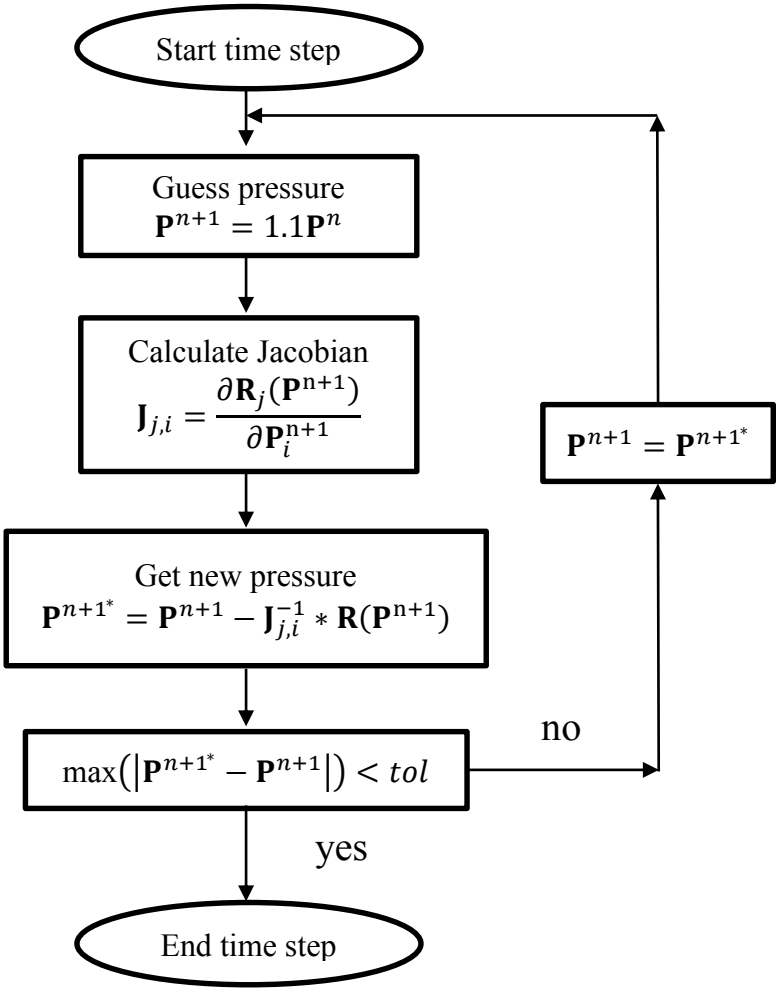

Figure 24. Schematic figure of Newton-Rapson algorithm in single-phase flow

3.3 Numerical examples

3.3.1 Verification of the model: Water flood scenario

To verify the two-phase fluid flow simulator used in this study is valid, we compared the multi-phase simulator with the commercial software. The case that we testified is water flooding in compressible oil reservoir. The reservoir consists of 15×15 grid blocks. Assume an isotropic heterogeneous permeability distribution which is given in a file named "permx.dat". There is one producer operating at a constant bottom-hole pressure of 2900 psi and one water injector which has a constant rate of injection of 300 bbl/day. The producer is located at grid block (15,15) and the injector is at (1,1). The well radius is 0.35ft. The properties needed are given in Table 7 and the equations are below.

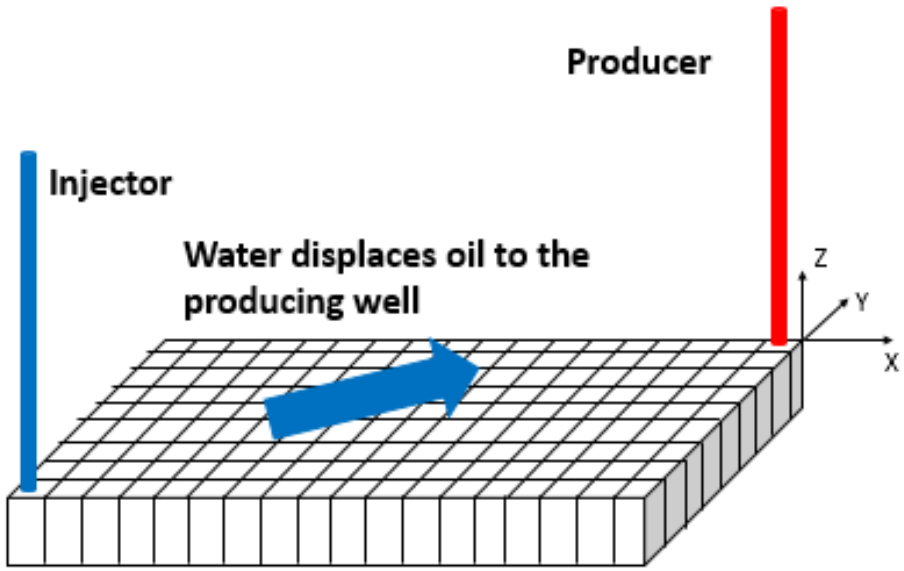

Figure 25. Schematic figure of numerical domain for water flood scenario

Table 7. Parameters used in Eclipse comparison

Model Properties	
Grid block in x direction	15
Grid block in y direction	15
Grid block in z direction	1
Grid block size in the x direction (ft)	30
Grid block size in the y direction (ft)	30
Grid block size in the z direction (ft)	30
Permeability (md)	"permx.dat"
Porosity	0.2
Pore compressibility (psi^{-1})	3e-6
Water Properties	
Formation volume factor	Exponential approximation
Viscosity (cp)	1
Compressibility (psi^{-1})	3e-6
Relative permeability	Table 8
Water density (lb/ft^3)	62.4
Oil Properties	
Formation volume factor	Table 9
Viscosity	Table 9
Compressibility	1e-5
Relative permeability	Table 8
Oil density (lb/ft^3)	45
Simulation Condition	
Initial pressure (psi)	3000
Bottom whole pressure (psi)	2900
Water injection rate (bbl/day)	300
Initial water saturation	0.25
Initial oil saturation	0.75

The permeability distribution from "permx.dat" in a log-scale is presented in Figure 26.

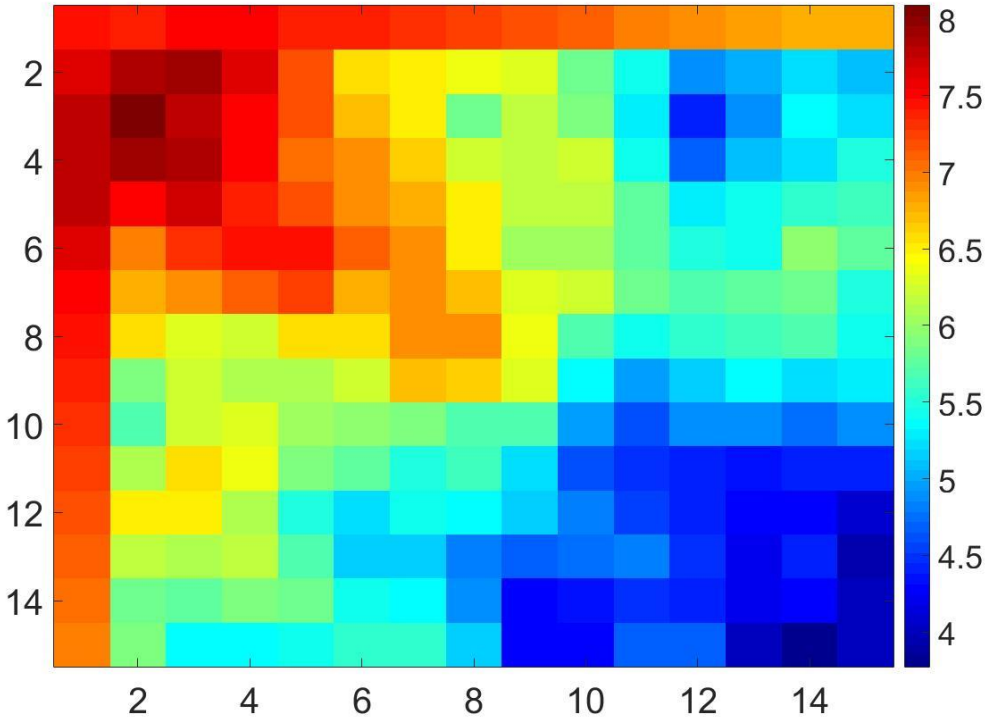

Figure 26. Permeability distribution in a log-scale.

Oil and water relative permeability equation is introduced in Table 8 below.

Table 8. Oil and water phase relative permeability equation and parameters

$K_{rw} = K_{rw}^{*}\left(\frac{S_w - S_{wr}}{1 - S_{or} - S_{wr}}\right)^2$	$K_{rw}(S_w \le S_{w,min}) = 0$	$K_{rw}(S_w \ge S_{w,min}) = K_{rw}^{*}$
$K_{ro} = K_{ro}^{*}\left(\frac{S_o - S_{or}}{1 - S_{or} - S_{wr}}\right)^3$	$K_{ro}(S_o \le S_{o,min}) = 0$	$K_{ro}(S_o \ge S_{o,min}) = K_{ro}^{*}$
$S_{wr} = 0.25$		
$S_{or} = 0.25$		
$S_{w,min} = S_{wr}$		
$S_{o,min} = S_{or}$		
$K_{ro}^{*} = 0.08$		
$K_{ro}^{*} = 0.7$		

With parameters and equations in Table 8, relative permeability trends of the water and the oil phase are graphed in Figure 27.

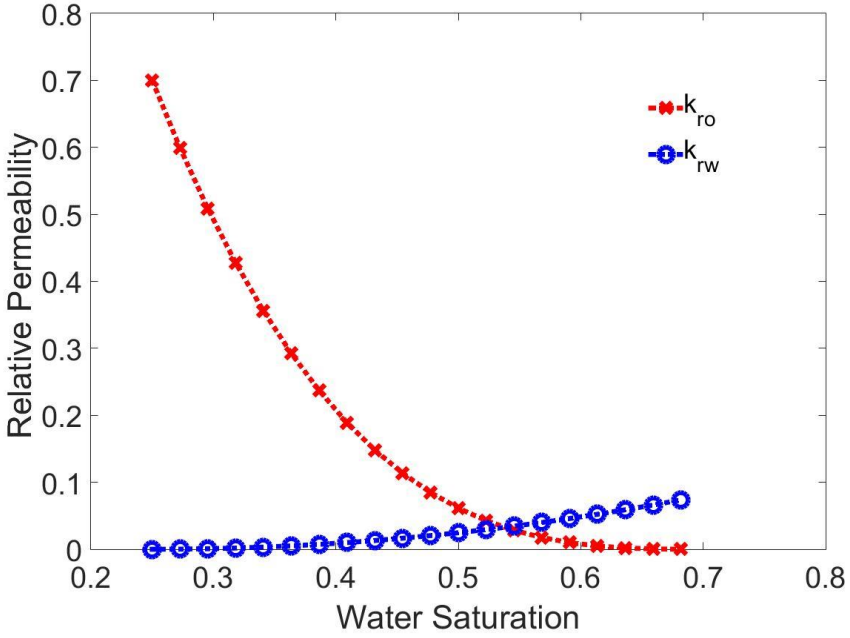

Figure 27. Relative permeability of water and oil phase with water saturation

The properties of dead oil with pressure are given in Table 9.

Table 9. Dead oil properties

Pressure	FVF(bbl/STB)	Viscosity(cp)
400	1.012	1.17
800	1.009	1.14
1200	1.005	1.11
1600	1.001	1.08
2000	0.996	1.06
2400	0.99	1.03
2800	0.988	1
3200	0.985	0.98
3600	0.98	0.95
4000	0.975	0.94
4400	0.97	0.92
4800	0.965	0.91
5200	0.96	0.9
5600	0.955	0.89

The simulation results are shown in the figures below.

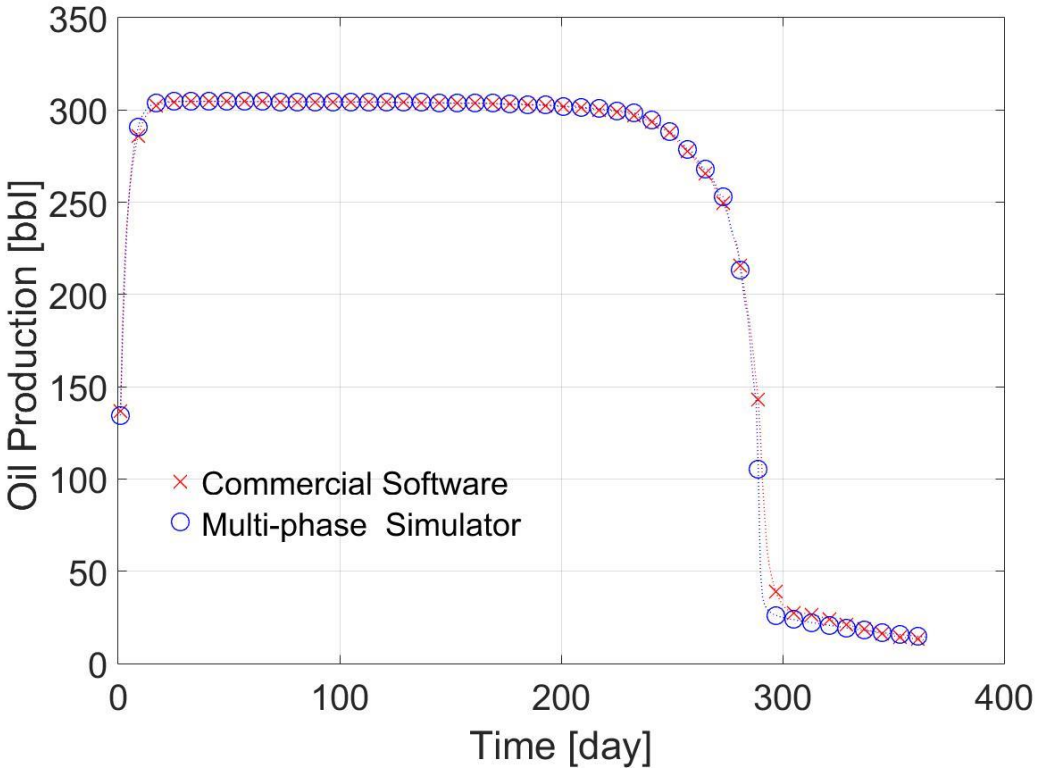

Figure 28. Oil production from Eclipse and the multi-phase flow simulator

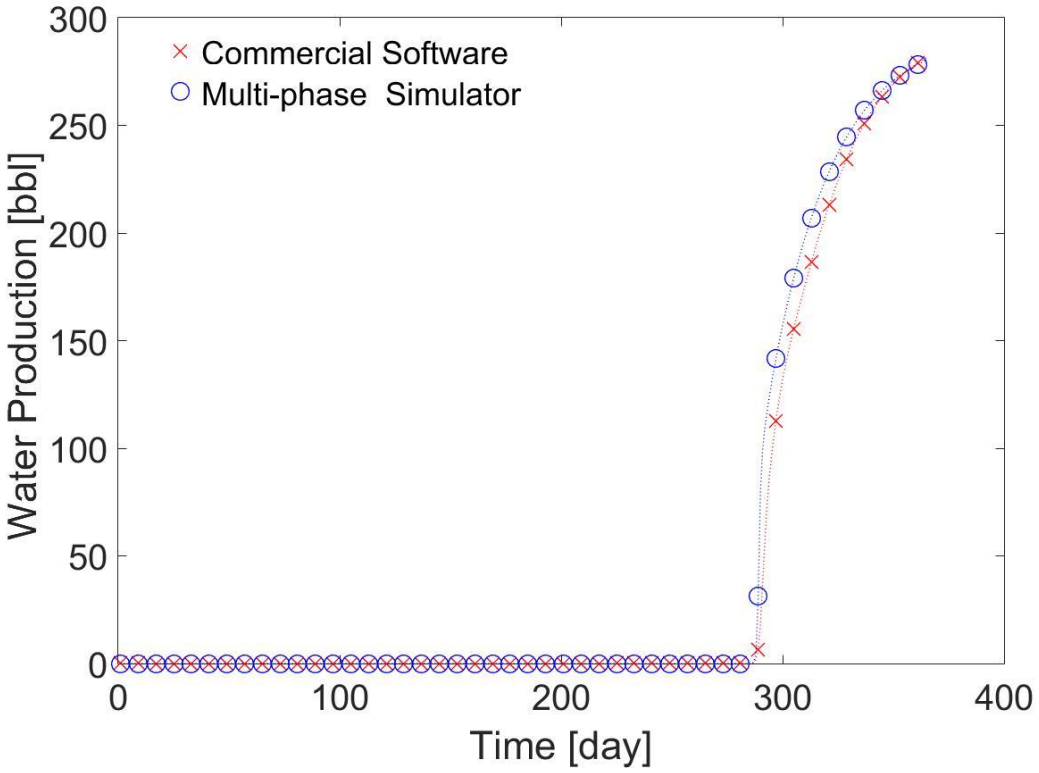

Figure 29. Water production from Eclipse and the multi-phase flow simulator

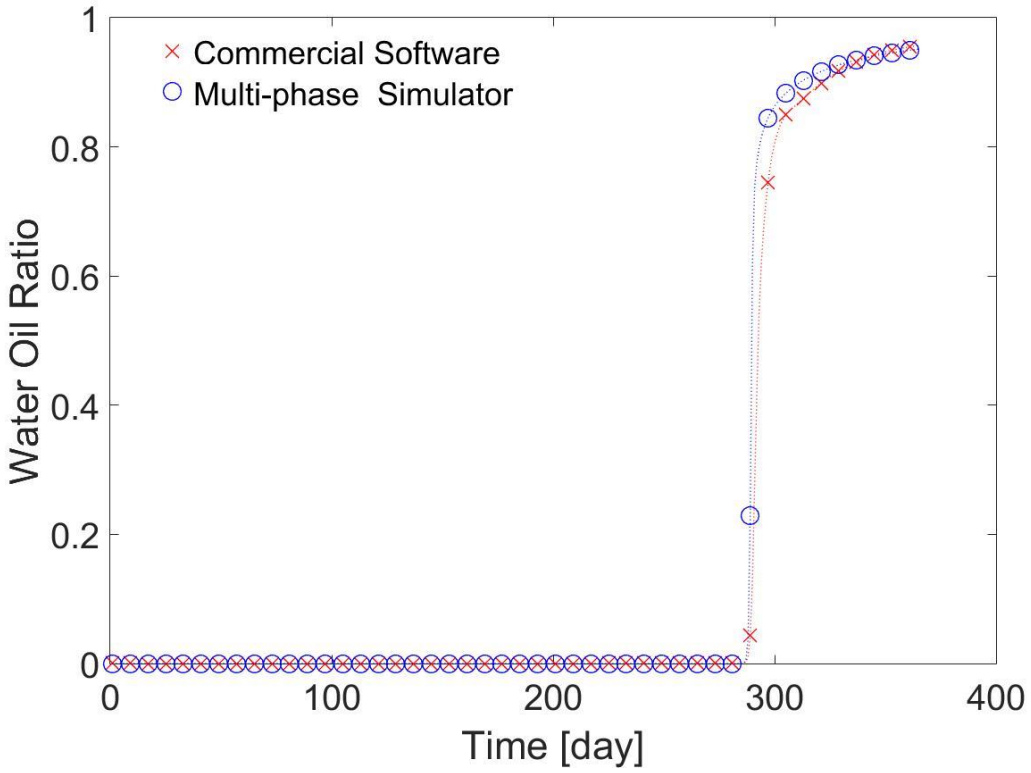

Figure 30. Water oil ratio from Eclipse and the multi-phase flow simulator

It is shown that the simulator is able to match the early time and the medium time response of the producer well in terms of oil and water production. The late response is promoted as the water breakthrough occurs earlier in our simulator than the commercial software. However, the trends of all cases are consistent in that the breakthrough occurs in advance and oil production starts to decrease ahead of the commercial software.

3.3.2 Verification of model: Production scenario

The multi-phase flow simulator is verified by simulating a single-phase flow case. The verification can be easily accomplished by setting the initial saturation of the targeting fluid to 1 and the others to 0. This means that the reservoir is fully water-saturated. Also, the maximum relative permeability of the targeting phase should be 1 in order to be consistent with a single-phase flow case. The schematic figure for the system which is used for verification is shown in Figure 31 below. It has 18 grid blocks in x-direction, 9 grid blocks in y-direction and 2 layers in z-direction. The producer is located in the first grid block in the top layer maintaining constant bottom whole pressure of 2900 psi. The domain has the same permeability, 5mD, and the porosity, 0.1, throughout the entire system. The configuration of the reservoir system is in Figure 31 and the specific parameters for the verification is in the table below.

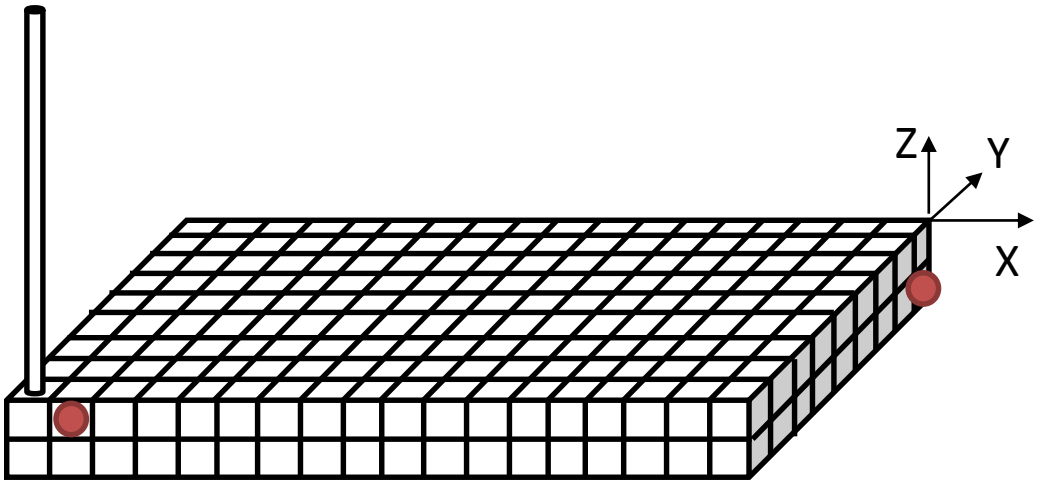

Figure 31. Numerical domain of the reservoir system in Sec.3.3.2.

It is noted that the grid block nearest to the wellbore(point 1) and the furthermost grid block from the wellbore(point 2) are selected to compare the pressure drop trends from the single-phase flow simulator and the multi-phase flow simulator. The results are presented in Figure 32 and Figure 33.

Table 10. Parameters used in Sec. 3.3.2

Model Properties	
Grid block in x direction	18
Grid block in y direction	9
Grid block in z direction	2
Grid block size in the x direction (ft)	30
Grid block size in the y direction (ft)	30
Grid block size in the z direction (ft)	30
Permeability (md)	5
Porosity	0.1
Pore compressibility (psi^{-1})	3e-6
Water Properties	
Formation volume factor	Exponential approximation
Viscosity (cp)	Exponential approximation
Compressibility (psi^{-1})	3e-6
Oil Properties	
Formation volume factor	Table 9
Viscosity	Table 9
Compressibility	1e-5
Relative permeability	Table 8
Oil density (lb/ft^3)	45
Simulation Condition	
Initial pressure (psi)	3500
Bottom whole pressure (psi)	2900
Total simulation time (day)	100

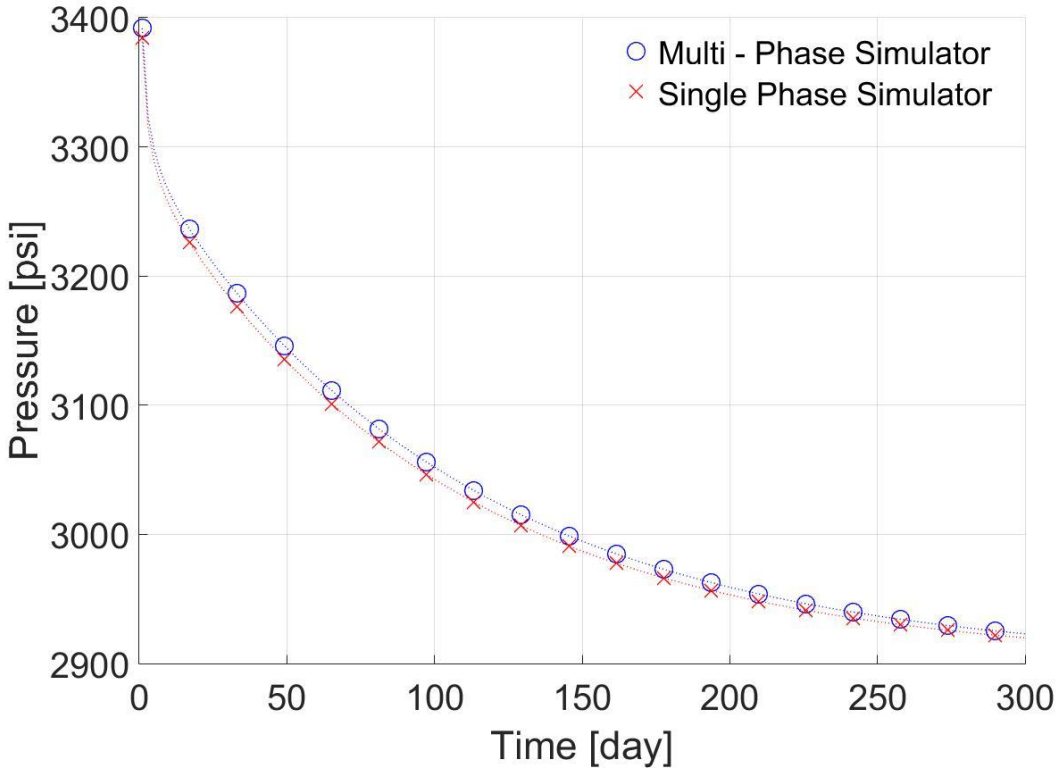

Figure 32. Pressure drop from the single and the multi-phase simulator at point 1

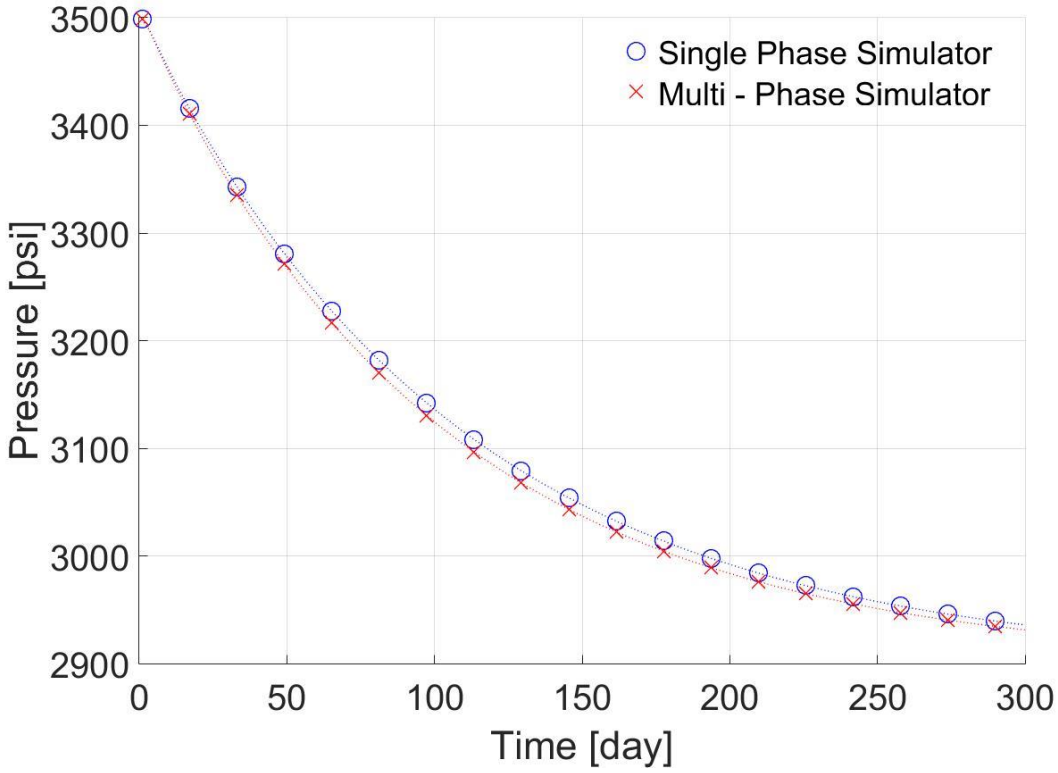

Figure 33. Pressure drop from the single and the multi-phase simulator at point 2

Both graphs show that the pressure drops from the single-phase simulator and the multi-phase simulator are well matched with each other. The maximum relative errors of both cases are less than 0.4%. It is assumed that the small differences shown in the middle region result from the Jacobian matrix.

3.3.3 Hydraulic fracture under in multi-phase flow: Initial water saturation

We then investigate the fracture propagation coupled to multi-phase flow. We first test the mesh-size dependency in the hydraulic fracture propagation model for the multi-phase flow system. We assume that there is 2.4 m of initial fracture and let the fracture propagate until it reaches 12 m of total fracture length. The system holds 40Mpa and 20C° of the initial pressure and temperature with 2.5×10^{-23} m^2 of permeability and 5×10^{-2} of porosity. The shear modulus and Poisson's ratio are 50GPa and 0.2. The injection rate is 4×10^{-5} m^3/s and the tensile strength is 2MPa. The size of the grid is 0.5 m × 1 m in y and z-direction yet it varies from 0.2 to 0.6 in x-direction. The size of the grid block in x-direction is presented in Table 11. From Figure 34 we find that the fracture propagation is almost the same, although we select different sizes of grid blocks.

Table 11. The grid sizes and the number of fractured grids

dx [m]	Number of initially fractured grid blocks	Total number of fractured grid blocks
0.2	12	60
0.3	8	40
0.4	6	30
0.6	4	20

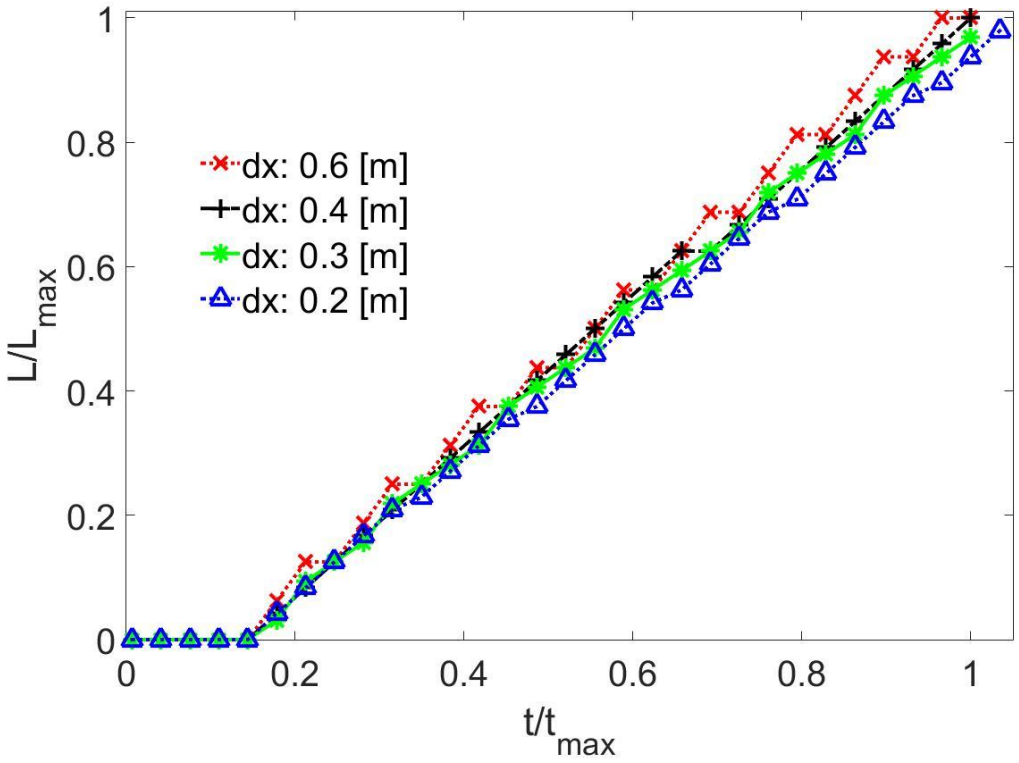

Figure 34. The grid size dependency of the hydraulic fracturing model

For the multi-phase flow system, the total fluid compressibility is given by the sum of saturation multiplied by fluid compressibility at each phase, as

$$c_f = s_l c_l \tag{109}$$

where s_l and c_l are saturation and the compressibility of phase l, respectively. In this study, the summation of water saturation and gas saturation is always one. Thus, high water saturation, which means low gas saturation, results in low total fluid compressibility.

On the other hand, low water saturation brings about high total fluid compressibility. To investigate how the saturation of phases affect fracture propagation, we perform numerical simulations at different initial water saturations. The sizes of grid blocks are uniform, 0.5m, 0.5m and 1m in x, y, z. The initial pressure and temperature of the reservoir are 40Mpa and 20C° with 2.5×10^{-23} m^2 of permeability and 5×10^{-2} of porosity. We have 5 initially fractured grid blocks near the wellbore to help fracture propagate. We inject water of 4×10^{-7} m^3/s to the reservoir, which holds 0.2, 50GPa of the Poisson's ratio and shear modulus respectively. The tensile strength of 0.1Mpa is used as fracture propagation criteria.

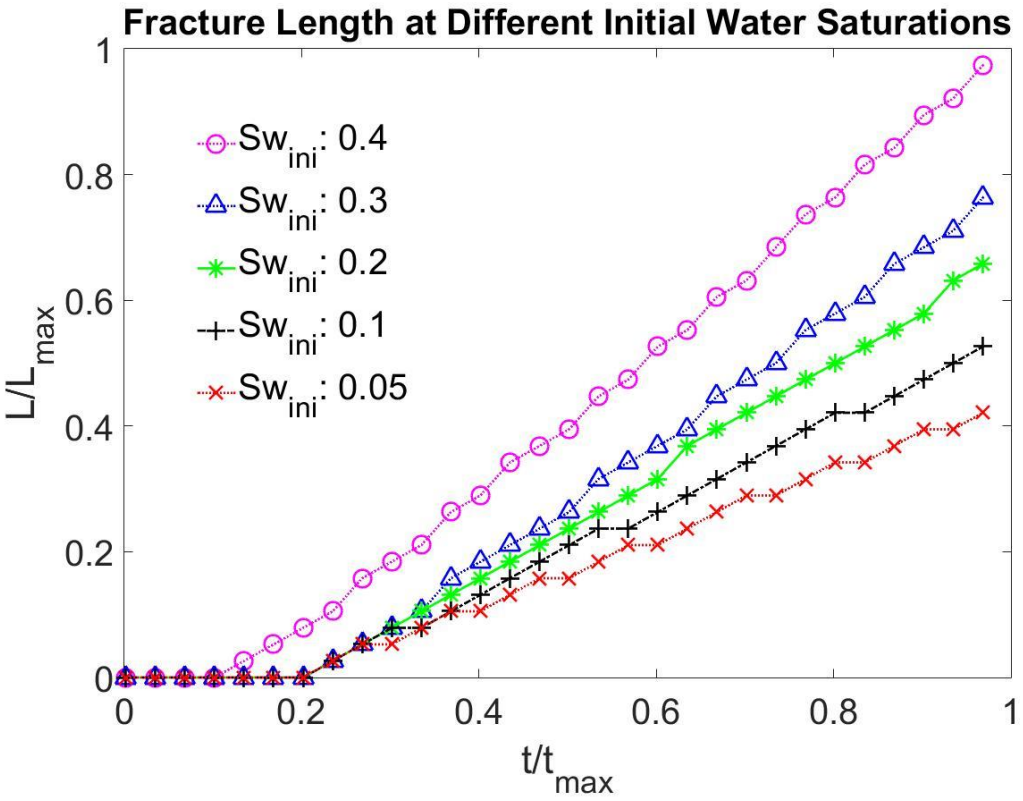

Figure 35. The fracture length at different initial water saturations

Figure 35 shows that the fracture propagation is delayed when the initial water saturation becomes lower. Note that $L_{\max}$ is utilized from the case of 0.4 initial water saturation, which holds the largest fracture length. As we found in Figure 14, the highly compressible fluid makes the total fracture length shorter. Similarly, in the water-gas flow system, the fracture would propagate slowly in the case of low water saturation, resulting in high total fluid compressibility.

3.3.4 Hydraulic fracture under in multi-phase flow: Gas concentration at the tip

Gas concentration at the hydraulic fracture tip is observed in our hydraulic fracture propagation model in water and gas flow system. Some studies (Adachi et al., 2007) suggests this phenomena by saying that there might be the gap between water front and the fracture tip. Let us call this gap as dry zone. The dry zone implies the existence of gas concentration at the fracture tip in two ways: 1. the movement of initial gas within the fracture to the fracture tip, 2. the possibility of leakage of the gas from the formation to the hydraulic fracture. This brings us to the fact that some part of the fracture near the fracture tip is partially filled with gas. As shown in Figure 36, there is less water at the fracture tip, implying the existence of the gas concentration at the tip. The case shown in Figure 36 has the system which holds 40Mpa and 20C° of the initial pressure and temperature with 2.5×10^{-23} m^2 of permeability and 5×10^{-2} of porosity. The shear modulus and Poisson's ratio are 50GPa and 0.2. The injection rate is 4×10^{-5} m^3/s and the tensile strength is 0.4MPa. The size of the grid is 0.5 m × 0.5 m × 1 m in x, y and z-direction. The residual gas saturation is 0.05.

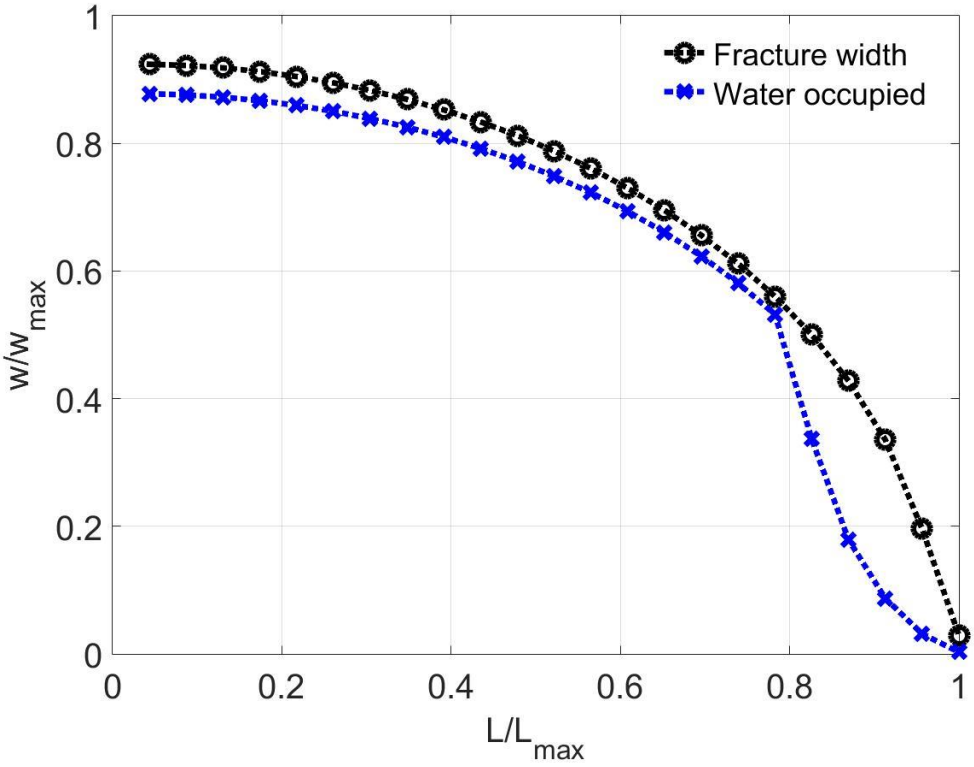

Figure 36. Fracture profile with water occupied in the fracture.

To further investigate the size of the dry zone near the fracture tip, we conduct sensitivity analysis on tensile strength and initial pressure of the reservoir. The numerical domain has 2 layers and one of the layer has 5 initially fractured grid blocks with injection point. We measure the fracture width and water saturation profile when the fracture reaches 18^{th} grid blocks.

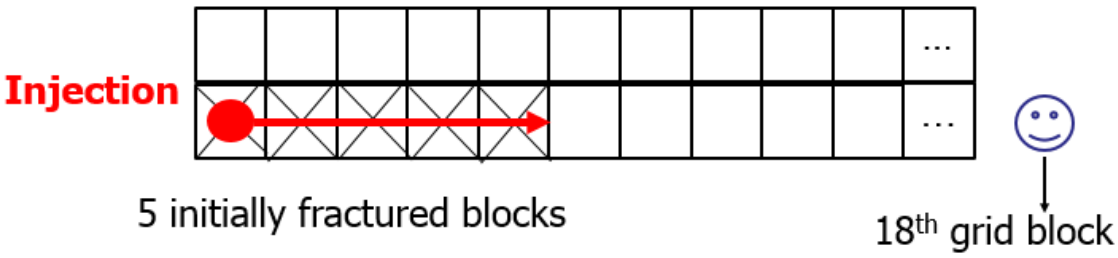

Figure 37. Schematics of numerical domain for the sensitivity analysis

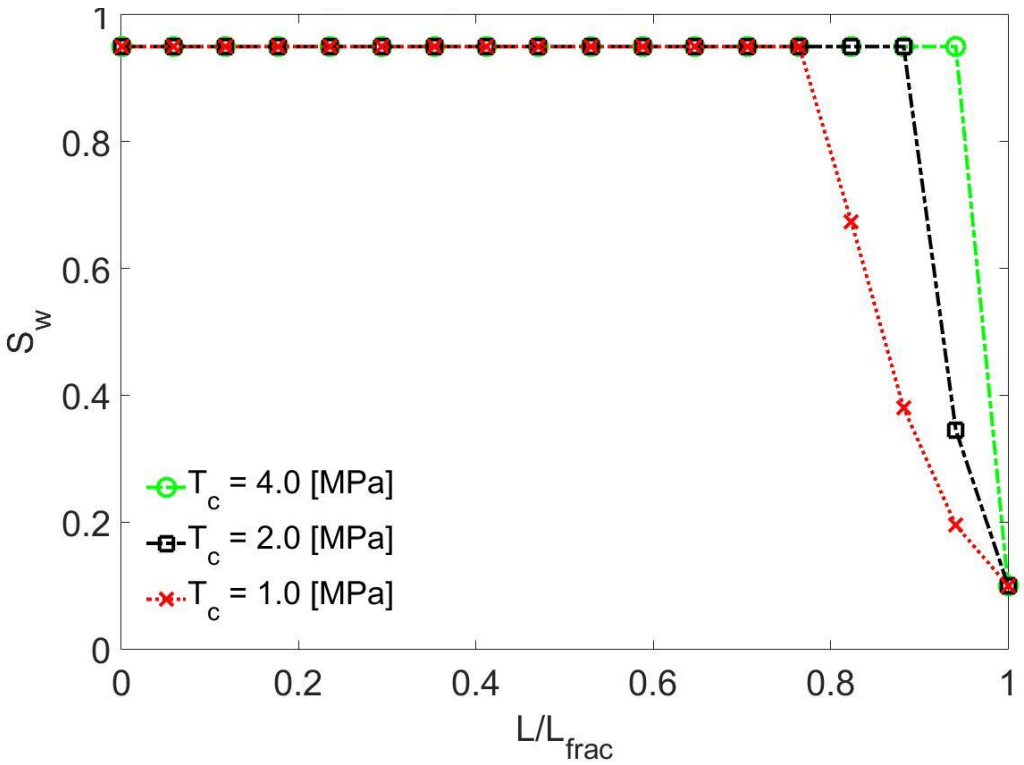

Figure 38. The water saturation profiles at different tensile strengths

The water saturation profile in Figure 38 shows that when tensile strength is low, the fracture near the tip is more saturated with gas, while the area closest to the injection well is almost saturated with water. This implies that, within the fracture, the initial gas near the injection well moves to the area near the fracture tip, due to its high mobility. Then, the water does not necessarily reach the fracture tip if the pressure is built up enough compared to the tensile strength when the fracture is extended. Also, when the fracture propagates quickly due to small tensile strength, the water flow may not catch up with the speed of the fracture propagation. Low relative permeability would be one of the factors that hinder the water from advancing.

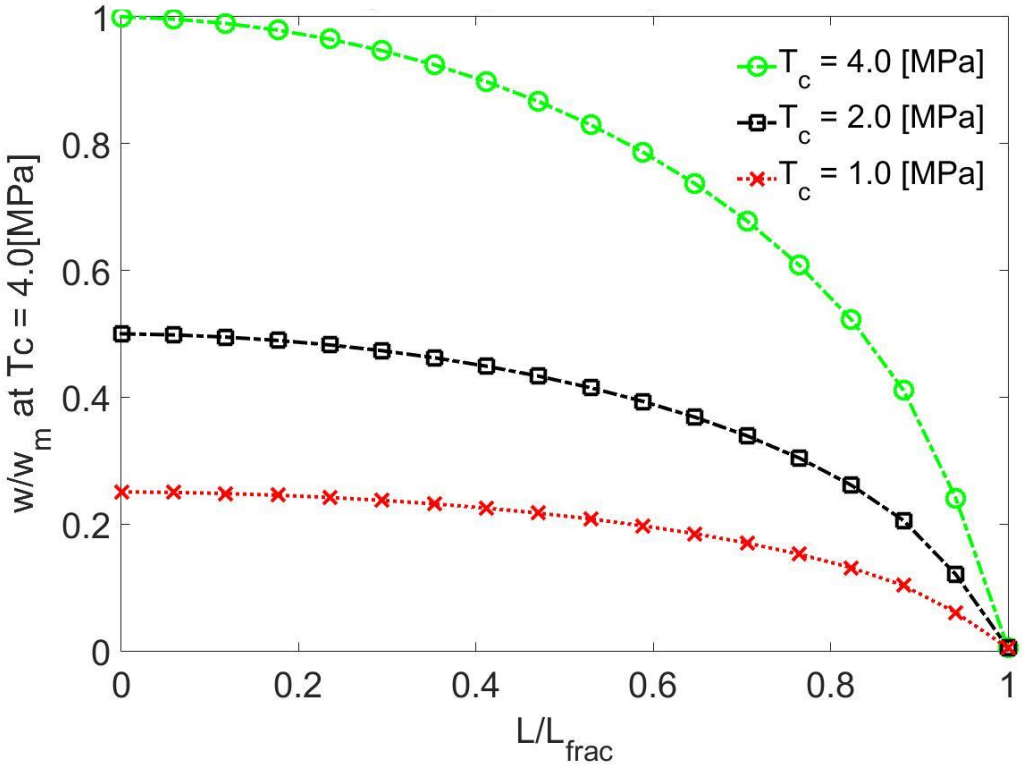

Figure 39. The fracture width profiles at different tensile strengths

Figure 39 shows the fracture width profiles at different tensile strengths. It is shown that the fracture width is highly dependent on tensile strength. We have large maximum fracture width when the tensile strength is large. This is because it requires large pore-pressure, which leads to greater displacement.

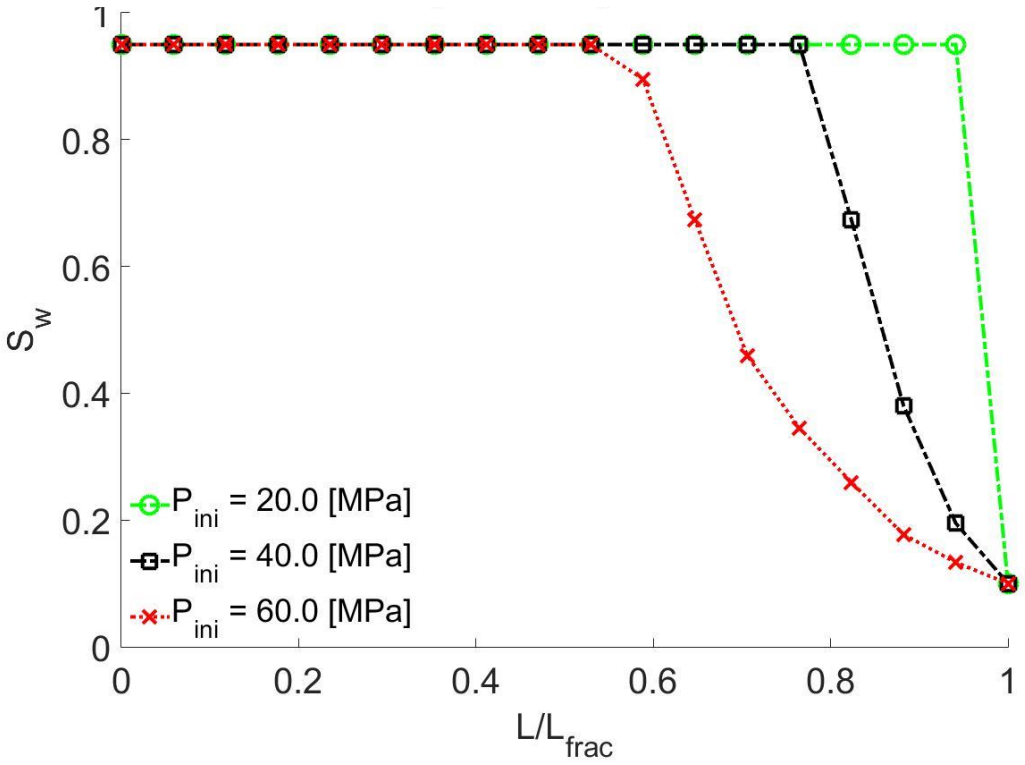

Figure 40. The water saturation profiles at different initial reservoir pressures

Next case is when the initial pressure of the reservoir is the only variable. It is shown that when the initial pressure of the reservoir is high, more gas concentration at the fracture tip is observed. The fact that when the initial pressure is high, it is easier for the fracturing fluid to be pressurized, leading fracture to propagate easily explains the observation. The quick fracture propagation increases the gap between the water front and fracture tip.

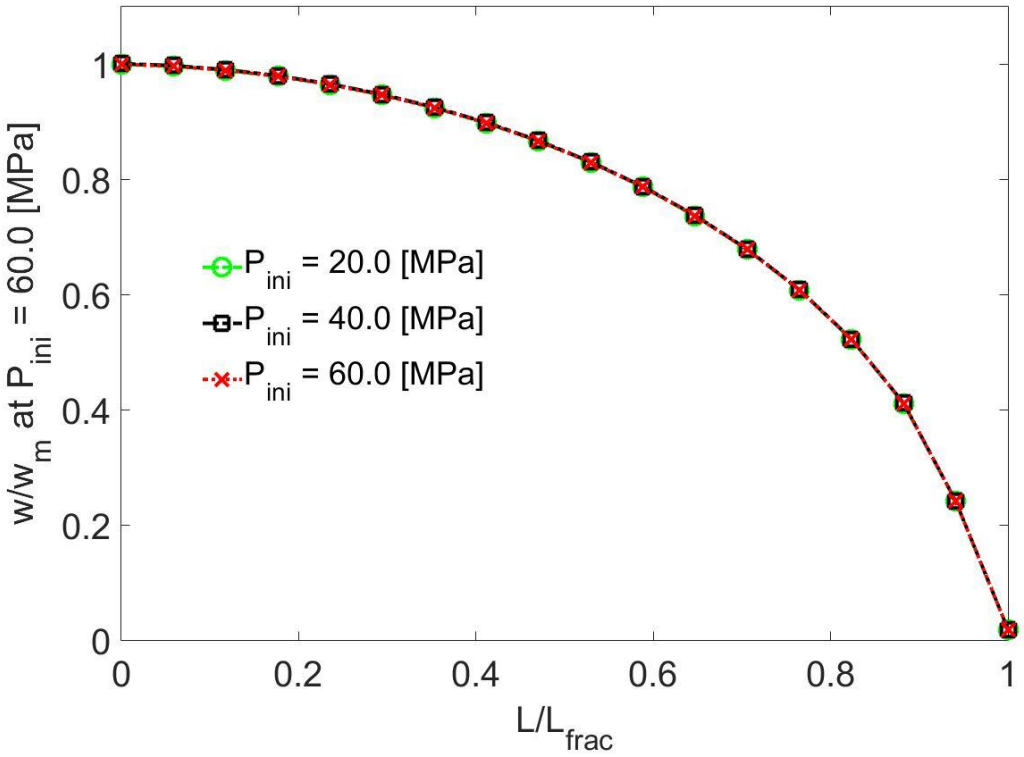

Figure 41. The fracture width profiles at different initial reservoir pressures

The fracture width profiles are all matched in the case that the initial pressure of the reservoir is the only variable because the tensile strengths at the all cases are same.

CHAPTER IV

SUMMARY AND CONCLUSIONS

We modeled a PKN fracture geometry numerically and compared the numerical results with its analytical solution. For the case that the fluid is compressible, we incorporated the fluid compressibility term, which has been ignored in previous studies. The results showed that as fluid becomes compressible, the fracture length and the maximum fracture width (i.e. the fracture width at the wellbore) decrease. We also studied the hydraulic fracturing process in a shale gas reservoir by using multi-phase flow and poromechanics. We performed numerical simulation, varying initial water saturation of the reservoir in order to investigate the effect of total fluid compressibility. We found that, for low initial water saturation, which yields high total fluid compressibility, the fracture propagates slowly.

For the multi-phase flow, we then investigated two possibilities that explain the existence of the dry zone: 1. the leakage of gas from the formation to the hydraulic fracture due to the vacuum area, 2. the movement of initial gas within the fracture to the fracture tip. We then identified gas concentration in near the fracture tip with sensitivity analysis.

Therefore, from numerical simulation of both single-phase and multi-phase flow, a rigorous modeling of flow coupled to geomechanics is highly recommended to predict propagation of the hydraulic fracture more accurately.

REFERENCES

Adachi, J., Siebrits, E., Peirce, A., & Desroches, J. (2007). Computer simulation of hydraulic fractures. *International Journal of Rock Mechanics and Mining Sciences*, *44*(5), 739-757.

Coussy O. (1995). *Mechanics of porous continua*. Chichester, England: John Wiley and Sons.

Detournay, E., Cheng, A. D., & McLennan, J. D. (1990). A poroelastic PKN hydraulic fracture model based on an explicit moving mesh algorithm. J. Ener. Resour. Tech., 112(4):224-230.

Detournay, E. (2004). Propagation regimes of fluid-driven fractures in impermeable rocks. *International Journal of Geomechanics* 4.1: 35-45.

Economides, M. J., & Nolte, K. G., Eds. (2000). *Reservoir Stimulation*. (p. 856). Chichester, England: John Wiley and Sons.

Ertekin, T., Abou-Kassem, J. H. K., Gregory, R., Turgay Ertekin, J. H., & Gregory, R. K. (2001). *Basic applied reservoir simulation* (No. Sirsi) i9781555630898).

Freeman, C. M., Moridis, G. J., & Blasingame, T. A. (2011). A numerical study of microscale flow behavior in tight gas and shale gas reservoir systems. *Transport in porous media* 90.1 (pp. 253-268).

Fu, Pengcheng, Scott M. Johnson, and Charles R. Carrigan. (2013). An explicitly coupled hydro-geomechanical model for simulating hydraulic fracturing in arbitrary discrete fracture networks. *International Journal for Numerical and Analytical Methods in Geomechanics* 37.14 (pp. 2278-2300).

Geertsma, J. (1966). Problems of rock mechanics in petroleum production engineering. *1st ISRM Congress*. International Society for Rock Mechanics.

Gidley, J. L. et al. (1989). Recent advances in hydraulic fracturing. SPE Monograph Series Vol. 12

Griffiths, S. K., Smith, C. W., & Nilson, R. H. (1984, June). Gas fracturing: Numerical calculations and field experiments. In *Proc. 25th Symp. on Rock Mechanics* (pp. 25-27).

Jeffrey, R. G. (1989, January). The combined effect of fluid lag and fracture toughness on hydraulic fracture propagation. In *Low Permeability Reservoirs Symposium*. Society of Petroleum Engineers.

Johnson, S. M., & Morris, J. P. (2009, January). Hydraulic fracturing mechanisms in carbon sequestration applications. In *43rd US Rock Mechanics Symposium & 4th US-Canada Rock Mechanics Symposium*. American Rock Mechanics Association.

Kemp, L. F. (1990). Study of Nordgren's equation of hydraulic fracturing.*SPE Production Engineering*, *5*(03), 311-314.

Kim, J., Tchelepi, H. A., & Juanes, R. (2011a). Stability and convergence of sequential methods for coupled flow and geomechanics: Drained and undrained splits. *Computer Methods in Applied Mechanics and Engineering*,*200*(23), 2094-2116.

Kim, J., Tchelepi, H. A., & Juanes, R. (2011b). Stability and convergence of sequential methods for coupled flow and geomechanics: Fixed-stress and fixed-strain splits. *Computer Methods in Applied Mechanics and Engineering*,*200*(13), 1591-1606.

Kim, J., & Moridis, G. J. (2012a, January). Modeling And Numerical Simulation For Coupled Flow And Geomechanics In Composite Gas Hydrate Deposits. In *46th US Rock Mechanics/Geomechanics Symposium*. American Rock Mechanics Association.

Kim, J., Sonnenthal, E. L., & Rutqvist, J. (2012b). Formulation and sequential numerical algorithms of coupled fluid/heat flow and geomechanics for multiple porosity materials. *International Journal for Numerical Methods in Engineering*, *92*(5), 425-456.

Kim, J., Moridis, G., Yang, D., & Rutqvist, J. (2012c). Numerical studies on two-way coupled fluid flow and geomechanics in hydrate deposits. *SPE Journal*, *17*(02), 485-501.

Kim, J., & Moridis, G. J. (2013). Development of the T+ M coupled flow–geomechanical simulator to describe fracture propagation and coupled flow–thermal–geomechanical processes in tight/shale gas systems. *Computers & Geosciences*, *60*, 184-198.

Kim, J., & Moridis, G. J. (2015). Numerical analysis of fracture propagation during hydraulic fracturing operations in shale gas systems. *International Journal of Rock Mechanics and Mining Sciences*, *76*, 127-137.

Min, K. B., Rutqvist, J., Tsang, C. F., & Jing, L. (2004a). Stress-dependent permeability of fractured rock masses: a numerical study. *International Journal of Rock Mechanics and Mining Sciences*, *41*(7), 1191-1210.

Min, K. B., Jing, L., & Stephansson, O. (2004b). Determining the equivalent permeability tensor for fractured rock masses using a stochastic REV approach: method and application to the field data from Sellafield, UK.*Hydrogeology Journal*, *12*(5), 497-510.

Nordgren, R. P. (1972). Propagation of a vertical hydraulic fracture. *Society of Petroleum Engineers Journal*, *12*(04), 306-314.

Park, J., Kim, J., (2016, June). Importance of fluid compressibility and multi-phase flow in numerical modeling of hydraulic fracture propagation. submitted. *50th Symp. on Rock Mechanics* .

Peng, D. Y., & Robinson, D. B. (1976). A new two-constant equation of state. *Industrial & Engineering Chemistry Fundamentals*, *15*(1), 59-64.

Perkins, T. K., & Kern, L.R. (1961). Widths of hydraulic fractures. J. Pet. Tech., 13(09):937-949.

Ramamurthy, G., & Hujeux, J. C. (1988). A Moving Mesh Integro Variational Formulation Applied to Hydraulic Fracturing. In *Computational Mechanics' 88*(pp. 1521-1522). Springer Berlin Heidelberg.

Schnürle, Philippe, & Char-Shine Liu. (2011). Numerical modeling of gas hydrate emplacements in oceanic sediments. *Marine and Petroleum Geology* 28.10: 1856-1869.

Selim, M. S., & Sloan, E. D. (1989). Heat and mass transfer during the dissociation of hydrates in porous media. *AIChE Journal* 35.6: 1049-1052.

Settari, A. (1989, January). Numerical modelling of hydraulic fracturing in underground rocks. In *ISRM International Symposium*. International Society for Rock Mechanics.

Settari, Antonin, & Mourits, F. M. (1998). A coupled reservoir and geomechanical simulation system. *Spe Journal* 3.03: 219-226.

Sun, X., & Mohanty, K. K. (2005). Simulation of methane hydrate reservoirs, SPE 93015. *2005 SPE Reservoir Simulation Symposium, Houston, TX USA*. Vol. 31. 2005.

Sneddon, I. N., & Lowengrub, M.(1969). Crack problems in the classical theory of elasticity. New York: Wiley.

Taron, J., Elsworth, D., & Min, K. B. (2009). Numerical simulation of thermal-hydrologic-mechanical-chemical processes in deformable, fractured porous media. *International Journal of Rock Mechanics and Mining Sciences*, *46*(5), 842-854.

Towler, Brian F.(2002). *Fundamental principles of reservoir engineering*. Vol. 8. Society of Petroleum Engineers.

Wang, J. H., Zhu, W. C., Wu, Y., Wei, C. H., & Liu, J. S. (2014, January). Impact of Rock-Gas Interactions on the Gas Fracturing Processes. In *ISRM International Symposium-8th Asian Rock Mechanics Symposium*. International Society for Rock Mechanics.

Wu, K., & Olson, J. E. (2015). Simultaneous multifracture treatments: fully coupled fluid flow and fracture mechanics for horizontal wells. *SPE Journal*,*20*(02), 337-346.

Yew, C. H., & Liu, G. H. (1993). The Fracture Tip and Critical Stress Intensity Factor of a Hydraulically Induced Fracture. *SPE production & Facilities*, *8*(03), 171-177.

Valko, P., & Economides, M. J. (1995). *Hydraulic fracture mechanics*. Wiley, New York.

APPENDIX

THE CONTINUITY EQUATION WITH FLUID COMPRESSIBILITY

In this appendix, the derivation of the local mass balance equation is presented. The mass balance equation is described as follows

$$\frac{\partial(\rho V)}{\partial t} + \nabla \cdot (\rho \vec{u} V) = 0 \tag{1}$$

where ρ is the fluid density, t indicates time, V is the control volume and $\vec{u}$ is the flow velocity. If we assume that the fluid density does not change with time and space, which means that the fracturing fluid is incompressible, then ρ can be canceled out in the first and second term. Noting that the control volume can be described as $V = w \times h_f \times dx$ yields

$$\frac{\partial V}{\partial t} + \nabla \cdot (\vec{u} V) = \frac{\partial(wHdx)}{\partial t} + \frac{\partial}{\partial x}\left(\frac{dx}{dt} wHdx\right) = 0 \tag{2}$$

It is worth noting that h_f is considered to be fixed and dx is also constant as we set so that they can come out from the derivatives and be canceled out. That leads Eq.(A.2) to

$$\frac{\partial w}{\partial t} + \frac{\partial q}{\partial x} = 0 \tag{3}$$

where q is volumetric flow rate per unit height of fracture. Note that Eq.(A.3) is identical to Eq.1 without leak-off term. If the density is the function of time and space depending

on the fluid pressure, which means that the fracturing fluid is compressible, the first temr in Eq.(A.1) becomes

$$\frac{\partial(\rho V)}{\partial t} = \rho \frac{\partial V}{\partial t} + V \frac{\partial \rho}{\partial t} = \rho \frac{\partial V}{\partial t} + V c_f \rho \frac{\partial p}{\partial t} \tag{4}$$

This is because $\partial\rho / \partial t = \partial\rho / \partial p \times \partial p / \partial t$ by chain rule and $\partial\rho / \partial p = c_f \times \rho$ from the definition of fluid compressibility.

$$c_f = \frac{1}{\rho} \frac{\partial \rho}{\partial p} \tag{5}$$

The second term of Eq.(A.1) in 1 dimensional problem yields to

$$\nabla \cdot (\rho \vec{u} V) = \frac{1}{\partial x} (\rho \vec{u} V) = \frac{1}{\partial x} (\rho \vec{u} (wHdx)) \tag{6}$$

Rearranging Eq.(A.1) by Adding Eq.(A.4) and Eq.(A.6) becomes

$$\rho \frac{\partial wHdx}{\partial t} + wHdx c_f \rho \frac{\partial p}{\partial t} + \frac{1}{\partial x} (\rho \vec{u} (wHdx)) = 0 \tag{7}$$

We can divide Eq.(A.7) with $h_f dx$ and let us assume that ρ does not change with space much so that we can make ρ out of the space derivative. This results in

$$\frac{\partial w}{\partial t} + w c_f \frac{\partial p}{\partial t} + \frac{\partial q}{\partial x} = 0 \tag{8}$$